Control Engineering Practice 144 (2024) 105818

Contents lists available at ScienceDirect

Control Engineering Practice

journal homepage: www.elsevier.com/locate/conengprac

# Experimental assessment of combined sliding mode & moment-based control ($SM^2C$) for arrays of wave energy conversion systems

Nicolás Faedo [a,*], Facundo D. Mosquera [b], Edoardo Pasta [a], Guglielmo Papini [a], Yerai Peña-Sanchez [c], Carolina A. Evangelista [b], Francesco Ferri [d], John V. Ringwood [e], Paul Puleston [b]

[a] Marine Offshore Renewable Energy Lab, Department of Mechanical and Aerospace Engineering, Politecnico di Torino, Turin, Italy
[b] Instituto de Investigaciones en Electrónica, Control y Procesamiento de Señales, Universidad Nacional de La Plata, Buenos Aires, Argentina
[c] Department of Mathematics, University of the Basque Country, Bilbao, Spain
[d] Department of the Built Environment, Aalborg University, Aalborg, Denmark
[e] Centre for Ocean Energy Research, Maynooth University, Maynooth, Ireland

ARTICLE INFO

*Keywords:*
Wave energy
Wave energy converters
Array
Farm
Optimal control
Moments
Moment-based theory
Sliding mode
Experimental assessment
Experimental validation

ABSTRACT

Motivated by the lack of comprehensive experimental implementation and assessment of the potential benefit that can be achieved with energy-maximising optimal control solutions for arrays of wave energy converters (WECs), we present, in this paper, the development, design, experimental implementation, and performance appraisal, of optimal moment-based control for arrays of WEC systems. Both centralised and decentralised controllers are evaluated. Four different WEC array layout configurations are considered, with up to three 1:20 scale prototypes of the Wavestar WEC system operating simultaneously within the basin, subject to a variety of sea state conditions. In particular, the proposed controller, termed *sliding-mode-moment-based controller* $SM^2C$, is composed of a receding-horizon moment-based reference generation process, and a subsequent proportional–integral–derivative-like continuous sliding mode tracking controller. This composite control structure is implemented and assessed experimentally, providing a detailed analysis of key performance metrics. We show that the proposed $SM^2C$ strategy is able to maximise energy absorption for all the considered WEC array layouts, with up to 2.8 times energy improvement when compared to the benchmark controller case. The findings of this experimental study show tangible proof of the performance enhancement that can be achieved in real arrays of WEC systems with the use of appropriate control technology, demonstrating not only the feasibility of the proposed $SM^2C$ strategy in itself, but the key role that control systems have to play in the pathway towards effective exploitation of the yet largely untapped wave energy resource.

## 1. Introduction

Predictions of an increase of around 50% of global energy requirements between 2018 and 2050 (Energy Information Administration (EIA), 2019) raises major concerns regarding future energy provision. Within this scenario, a great deal of attention and interest has lately shifted to the effective and efficient use of renewable energy sources, inherently pushed by a growing awareness of the social and environmental challenges posed by fossil energy, and pressure to honour emission limits in the pathway towards a low-carbon energy society (European Commission, 2011, 2014, 2019, 2022).

Ocean renewable energies are widely recognised for their potential to provide significant support in the quest for sustainable and renewable energy sources. This has, naturally, generated interest from governments, public entities, developers, and investors, who are eager to accelerate the pathway towards harnessing the many advantages of this renewable source. Among ocean renewables, *wave energy* has a vast untapped potential, estimated to be around 30,000 TWh/year (Gunn & Stock-Williams, 2012; Mork, Barstow, Kabuth, & Pontes, 2010; Reguero, Losada, & Méndez, 2015). Wave energy has several advantages over other renewable sources, including its higher density compared to solar and wind power (McCormick, 2013), availability up to 90% of the time (López, Andreu, Ceballos, Alegría, & Kortabarria, 2013), high predictability (Sasaki, 2017), and minimal impact on the ocean environment when harnessed properly (Copping et al., 2020; Langhamer, Haikonen, & Sundberg, 2010).

Although attempts to harness wave energy have been made since the 19th century (Ross, 1995), commercial harvesters are not yet widely available (Guo & Ringwood, 2021). This is due to several

* Corresponding author.
*E-mail address:* nicolas.faedo@polito.it (N. Faedo).

https://doi.org/10.1016/j.conengprac.2023.105818
Received 12 June 2023; Received in revised form 20 September 2023; Accepted 4 December 2023
Available online 14 December 2023

factors, including the unpredictable nature of waves depending on location, the harsh environment that the harvesters must withstand, and a lack of convergence on the optimal design for wave energy converters (WECs). As a result, the cost of energy from WECs is generally higher than that of sister renewable sources (Guo & Ringwood, 2021; Ringwood, 2022; Trueworthy & DuPont, 2020), making commercial viability challenging.

Within the field of wave energy technology, it is already well known and accepted that a major reduction in the levelised cost of energy (LCoE) is crucial for achieving large-scale commercialisation, which can be accomplished through two main steps. The first key enabler is the development and use of suitable *control system technology*, which can maximise the energy extracted by WEC systems from the wave resource, while also accounting for the underlying physical limitations of WEC devices (Faedo, Olaya, & Ringwood, 2017; Ringwood, Bacelli, & Fusco, 2014). The control problem for WEC systems essentially involves optimal computation of the force (or torque) exerted by the power take-off (PTO) system on the converter, to maximise the associated energy conversion output, based on the current wave conditions. The degree of performance enhancement that can be achieved through appropriate control can be significant, with multipliers reported in the range from 2 to 3 (see *e.g.* Babarit & Clément, 2006; Faedo, García-Violini, Peña-Sanchez and Ringwood, 2020; Faedo et al., 2023), depending on the particular WEC device, PTO system, wave climate, and control algorithm used (Ringwood, 2020).

To achieve cost reduction and meet installed capacity demands, deploying WEC systems in *arrays* (also often referred to as WEC 'parks' or 'farms') is the second crucial factor in lowering the associated LCoE, in addition to the effective use of appropriate control technology. This involves the systematic deployment of multiple WEC systems in a common ocean area, in row/column-like arrangements, generating specific layouts. The purpose of this is to reduce costs associated with installation, operation, and maintenance per device, and effectively achieve the required installed capacity. A comprehensive understanding of the behaviour of WEC arrays is therefore essential to optimise their arrangement (layout) for efficient farm configurations (Göteman, Giassi, Engström, & Isberg, 2020; Hodges et al., 2021; Robertson, Hiles, Luczko, & Buckham, 2016; Ruehl & Bull, 2012).

Though it is clear that both control technology and array deployment are fundamental to achieving commercial reality, merging these two key stepping stones, in such a way as to exploit their synergies, is not a particularly simple task. When multiple WEC devices are installed in an array configuration, these inevitably interact with each other, since each device has the ability to alter the surrounding wave field, which in turn affects the hydrodynamics of neighbouring devices (see *e.g.* Babarit, 2013). As such, consideration of these interactions can become particularly relevant within the control design procedure, effectively having an impact on final performance (in terms of energy absorption), and hence optimal layout configurations. Crucially, WEC arrays have the potential to create *constructive* (if the interaction is well managed by an array control system) as well as *destructive* interference, which is typical in wind farms.

Early studies in WEC array control can be found in Evans (1979) and Thomas and Evans (1981), based upon frequency-domain optimal conditions (*i.e.* the so-called impedance-matching principle, see *e.g.* Carapellese, Pasta, Paduano, Faedo, & Mattiazzo, 2022; Faedo, Carapellese, Pasta and Mattiazzo, 2022; Faedo et al., 2022). We note that Thomas and Evans (1981) effectively incorporates motion constraints into the control design procedure being, to the best of our knowledge, the first result with practical impact proposed within the state-of-the-art of WEC array control. Contemporary studies often include more sophisticated control techniques, in either decentralised (often also called 'independent'), or centralised (often referred to as 'global') control formulations. Within the WEC array case, the term decentralised is used for controllers which 'ignore' the hydrodynamic interactions between devices in the array, and hence the associated control computation depends on the dynamics of a single device only. While less computationally demanding, this can often lead to suboptimal performance in terms of energy absorption, especially if the devices are located reasonably close to each other for economic purposes (*e.g.* sharing of mooring systems and minimisation of electrical cabling). Centralised controllers, in contrast, aim to incorporate the complete hydrodynamic interactions affecting the WEC array, providing superior performance with respect to their decentralised counterparts. There is, clearly, a price to pay in terms of computational burden, which can often preclude real-time implementation, particularly in the case of controllers involving an online optimisation procedure, such as *e.g.* centralised MPC-based solutions (Li & Belmont, 2014; Oetinger, Magaña, & Sawodny, 2015; Zhang et al., 2022; Zhong & Yeung, 2019, 2022). An improvement in computational efficiency, for this centralised case, can be achieved by means of tailored control parameterisations, such as those offered by *e.g.* spectral/pseudospectral methods (Bacelli, Balitsky, & Ringwood, 2013; Bacelli & Ringwood, 2013; Garcia-Rosa, Bacelli, & Ringwood, 2015; Westphalen, Bacelli, Balitsky, & Ringwood, 2011), and (recently) moment-based theory (Faedo, Scarciotti, Astolfi and Ringwood, 2019; Faedo, Scarciotti, Astolfi, & Ringwood, 2021a). The latter, which is based on the mathematical notion of *moments* (Astolfi, 2010; Astolfi, Scarciotti, Simard, Faedo, & Ringwood, 2020), presents a number of advantages with respect to spectral/pseudospectral, offering *e.g.* guarantees of existence and uniqueness of control solutions via direct transcription of the centralised energy-maximising control problem for WECs into an associated finite-dimensional convex quadratic program (QP). Furthermore, moment-based control for WEC systems has been recently validated experimentally in Faedo et al. (2023) for a single WEC, showing a significant improvement with respect to benchmark controllers.

The large pool of control solutions for WEC arrays, including all those referenced in the previous paragraph, are typically tested within simulation (numerical) scenarios in idealised conditions (virtually with exactly the same control design and numerical simulation models), automatically hindering a realistic assessment of the potential increase in power absorption offered by such technology in the array case. Exceptions dealing with experimental implementation and assessment of (very simple) control solutions for WEC arrays do exist, in Stratigaki et al. (2014), Thomas et al. (2018) and Vervaet et al. (2022). Thomas et al. (2018) presents a simplified latching strategy for a set of four buoys, arranged in a single (horizontal) layout. As a matter of fact, this horizontal arrangement is mandatory for effective implementation of the explored latching strategy, since the 'central' WEC is employed to measure the incoming wave and determine the corresponding crests and troughs. With respect to Stratigaki et al. (2014), we note that most of the effort in Stratigaki et al. (2014) has focussed on characterising the resulting (modified) wave field, for diverse WEC array configurations, aiming at producing a dataset for numerical model validation, and hence is not a control-oriented study. Crucially, the devices in Stratigaki et al. (2014) have been tested without PTO system, and a simple mechanical damping has been fashioned for each prototype, to emulate a proportional (passive — see also Section 5) control action, without measured information on power absorption. The study in Vervaet et al. (2022), in contrast, considers an impedance-matching-based proportional–integral (PI) solution for energy-maximisation in a fixed array layout configuration, with two devices located within the basin at a fixed separation distance. The design of the PI controller is performed both in a centralised and decentralised control fashion, showing an associated improvement in the centralised case. Though effectively experimental, the study in Vervaet et al. (2022) is limited both in terms of the controller complexity considered, and the number of layouts/array configurations tested, hindering an assessment of the actual energy absorption enhancement that can be achieved with more sophisticated control technology, or alternative array configurations.

Driven by the absence of a comprehensive experimental implementation and assessment concerning the potential advantages attainable

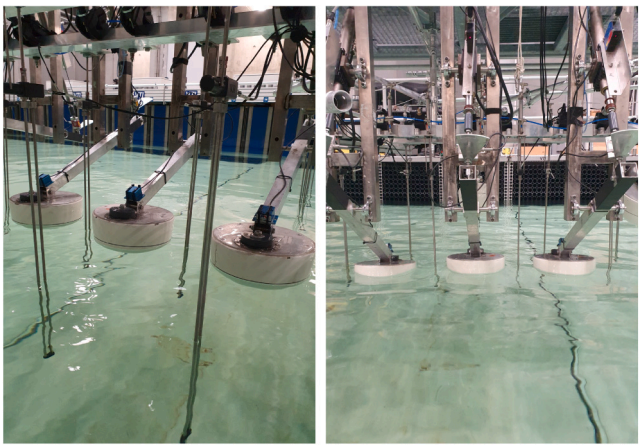

**Fig. 1.** Photographs of the experimental setup designed for the WEC array experimental campaign, from different angles. In this case, all three devices are present within the basin.

through energy-maximising optimal control solutions for WEC arrays, we present, in this study, the development, design, experimental implementation, and performance appraisal, of optimal moment-based control for arrays of WEC systems, in both *centralised* and *decentralised* fashion. As a matter of fact this is, to the best of our knowledge, the first study addressing the implementation and performance assessment of energy-maximising optimal control to a large set of WEC array cases, including diverse levels of interaction between devices. Based on a 1:20 scale prototype of the well-known Wavestar system (as depicted in Figs. 1 and 3), we consider the moment-based direct transcription solution developed in Faedo et al. (2021a), for four different WEC array layout configurations, in an experimental campaign conducted in the wave tank facilities available at Aalborg University (Denmark), involving up to 3 devices simultaneously operating within the basin. We note that the choice of this experimental system is not arbitrary, and is motivated by the large number of previous studies available on the (isolated) prototype (Heo & Koo, 2021; Ransley et al., 2017; Tom, Ruehl, & Ferri, 2018; Windt et al., 2020), being also featured as the baseline system for the Wave Energy Control Competition (WEC$^3$OMP) (Ringwood et al., 2019). As such, vast, transparent, and (virtually always) public information is readily available for this prototype within the WEC literature.

Specifically, within this study, motivated by the encouraging recent results presented in Mosquera, Faedo, Evangelista, Puleston, and Ringwood (2022) (numerical) and Faedo, Mosquera, Evangelista, Ringwood and Puleston (2022) (experimental – hardware-in-the-loop), a composite energy-maximising control structure is considered: the moment-based direct transcription technique in Faedo et al. (2021a) is used to generate a set of optimal (motion) references in a receding-horizon fashion (following the theoretical framework in Faedo, Peña-Sanchez and Ringwood (2020)), which are subsequently followed (*i.e.* tracked) *robustly* by means of sliding mode control. The choice of this composite loop, as opposed to other relatively standard techniques in the WEC field (see the discussion provided earlier within this section), is motivated by its efficiency in uncertain scenarios: In particular, the family of controllers based on sliding modes are virtually insensitive to modelling uncertainty, once the corresponding sliding manifold is reached (see *e.g.* Utkin, 2013). This characteristic is ideal for the WEC case where, given the inherent complexity behind hydrodynamic WEC modelling, the presence of uncertainty within control-oriented models is effectively ubiquitous (Windt, Faedo, Penalba, Dias, & Ringwood, 2021), and can be detrimental in controlled scenarios. In particular, we consider the continuous-time sliding-mode controller proposed in Pérez-Ventura, Mendoza-Avila, and Fridman (2021) which, as explicitly demonstrated within this manuscript (see Section 5), effectively achieves robust following of the computed energy-maximising profiles, hence guaranteeing optimal operation of each WEC layout and sea-state considered within this experimental campaign, and remarkable performance. Throughout our study, the combination of these two techniques, *i.e.* the composite control structure comprising moment-based optimal profile generation and sliding-modes tracking, is termed SM$^2$C (*sliding-mode-moment-based controller*). We show that the proposed SM$^2$C technique is able to maximise energy absorption consistently, in all the tested WEC array layouts and operating sea-state conditions.

Furthermore, given that optimal moment-based reference generation within SM$^2$C leverages a mathematical representation of the WEC array for effective computation of the energy-maximising profiles via direct transcription, we pursue a black-box system identification approach, to experimentally identify a set of dynamical models characterising each tested WEC array layout. This is performed by tailored design of input–output (I/O) tests, both for system identification, and subsequent model validation, within all the sea state conditions considered. The models obtained via the outlined system identification process are subsequently exploited for the design and tuning of the proposed SM$^2$C accordingly. Finally, we note that the performance of the proposed SM$^2$C strategy is compared to a benchmark control solution for WEC arrays, with the former showing an increase in energy absorption of up to 2.8 times that obtained with the latter.

The remainder of this paper is organised as follows. Section 1.1 introduces the notation used throughout our study. Section 2 details the experimental setup considered, including hardware, WEC array layouts tested, and wave conditions for evaluation of the implemented controllers, generated within the basin. Section 3 describes the experimental modelling procedure followed for black-box system identification of each WEC layout considered, including system passivation, and model validation for the considered sea states tested within the basin. Section 4 details the SM$^2$C, including moment-based reference generation, and subsequent tracking via continuous sliding mode control, describing each key parameter comprising the composite control structure.

### 1.1. Notation and preliminaries

The set of non-negative real values is denoted as $\mathbb{R}^+$, while $\mathbb{C}_{<0}$ and $\mathbb{C}^0$ denote the sets of complex values with negative and zero real part, respectively. Unless otherwise stated, if $x \in \mathbb{C}^n$, the notation $x_j \in \mathbb{C}$ denotes the $j$th entry of $x$. The notation $\lambda(A)$, with $A \in \mathbb{C}^{n\times n}$, is used for the set of eigenvalues of $A$. If $A = A^\star$, with $^\star$ the Hermitian transpose operator, $\lambda_{\min}(A) \in \mathbb{R}$ is used to denote the minimum eigenvalue associated with the Hermitian matrix $A$. The Hermitian part of $A$ is denoted (and defined) as $\mathscr{H}(A) = \frac{1}{2}(A + A^\star)$. The notation $\mathbb{N}_K$ is used for the set of natural numbers up to $K$, *i.e.* $\mathbb{N}_K = \{1, \dots, K\} \subset \mathbb{N}$. The symbols $\odot$ and $\oslash$ are used for the Hadamard product and division, respectively, while the notation $\otimes$ is used for the standard Kronecker product. The symbols $\mathbb{I}_N \in \mathbb{C}^{N\times N}$ and $\mathbb{1}_N \in \mathbb{R}^N$ denote the identity elements of the spaces $\mathbb{C}^{N\times N}$ and $\mathbb{C}^N$, considering standard and Hadamard matrix products, respectively. $F(s)$ and $F(\jmath\omega)$ are used for the Laplace and Fourier transform of the function $f$, provided these are well-defined. Given $\{f, g\} \subset L^2(\Xi)$, $\Xi \subset \mathbb{R}$, their standard inner product is denoted (and defined) as $\langle f, g\rangle_\Xi = \int_\Xi fg\,\mathrm{d}t$. The direct sum of $N$ matrices $A_i \in \mathbb{R}^{n\times n}$ is denoted as $\bigoplus_{i=1}^N A_i = \mathrm{diag}(A_1, \dots, A_N) \in \mathbb{R}^{nN\times nN}$. Given a matrix $M \in \mathbb{R}^{n\times m}$ the vectorisation operation on $M$ is denoted as $\mathrm{vec}(M) \in \mathbb{R}^{nm}$. Finally, the notation $\lceil x\rfloor^n$, with $x \in \mathbb{R}$, $n \in \mathbb{Q}$, is used for the signed power $n$ of $x$, *i.e.* $\lceil x\rfloor^n = |x|^n \mathrm{sign}(x)$, where we note that $\lceil x\rfloor^0 = \mathrm{sign}(x)$.

## 2. Experimental setup and operating conditions

This section is dedicated to providing a detailed description of the experimental setup considered, as presented in the photograph in Fig. 1, including the Aalborg University wave tank specifications,

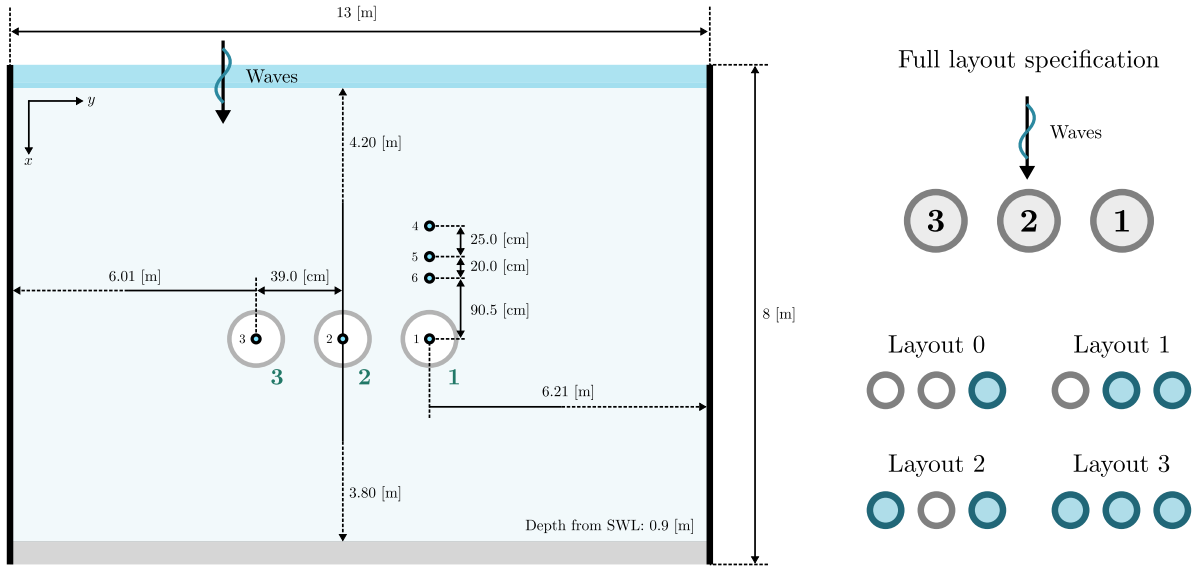


**Fig. 2.** Schematic representation of the wave basin at the Ocean and Coastal Engineering Laboratory, in Aalborg University. The schematic includes the position associated with each device within the tank, and the location of the wave gauges used for free-surface elevation acquisition (cyan-numbered circles). To test the different array layout configurations, each single prototype can be lifted out of the basin manually. The acronym SWL stands for still water level. (For interpretation of the references to colour in this figure legend, the reader is referred to the web version of this article.)

baseline WEC system, equipment associated with each device, wave gauge positions within the wave tank, and the considered WEC array layout specifications within this energy-maximising experimental control study.

### 2.1. Wave tank specifications

The wave tank facilities, considered within this experimental campaign, are those available at the Ocean and Coastal Engineering Laboratory at Aalborg University, Denmark. The dimensions associated with the basin are as described in the schematic presented[1] in Fig. 2. In particular, the available facilities comprise a basin of 19.3 [m] × 14.6 [m] × 1.5 [m] (length × width × depth), with an active testing area of 13 [m] × 8 [m] (length × width). The wave tank is equipped with a state-of-the-art long-stroke segmented wavemaker system with active absorption, composed of 30 individually controlled wave paddles, capable of producing a large variety of sea state conditions with high accuracy (see VTI, 2023). Within this study, the water depth within the tank has been fixed to 0.9 [m], while the wavemaker is set to generate long-crested waves, *i.e.* parallel with respect to (w.r.t.) the $y$-axis, and with a direction of 0° on the $x$-axis, as indicated within Fig. 2.

### 2.2. Prototype WEC and acquisition system

The baseline WEC system, chosen for this array experimental campaign, is a 1:20 scale Wavestar wave energy conversion system (Hansen & Kramer, 2011). The single unit of this prototype, illustrated in Fig. 3, comprises a floater mechanically hinged to an out-of-the-water fixed reference point (point **A** in Fig. 3). At the equilibrium position, the floater's arm stands at approx. 30° w.r.t. the still water level (SWL). Note that the WEC is free to move in a single DoF. The main set of parameters associated with the single baseline prototype can be found in Table 1. The PTO (actuator) system is an electrical, direct-drive, linear motor (*LinMot Series P01-37 x 240F*), sitting on the upper structural joint composing the device (see Fig. 3). The corresponding drive is a *LinMot E1200*, with a force rating up to ±200 [N].

[1] Note that Fig. 2 is simply a schematic representation of the setup, and objects are not to scale with respect to the tank dimensions.

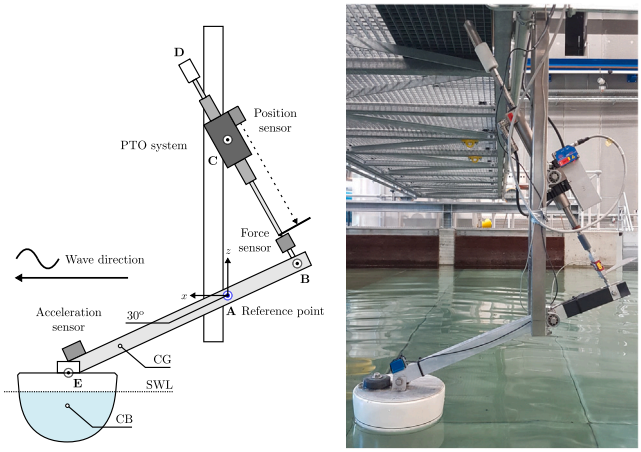


**Fig. 3.** Photo of the baseline Wavestar prototype unit for the WEC array experimental campaign (right) and associated schematic representation (left). The acronym SWL stands for still water level.

Although translational displacement (in the linear generator degree of freedom) can be directly obtained as an output of the PTO driver, it is also measured via a dedicated laser position sensor (*MicroEpsilon ILD-1402-600*) for redundancy (see Fig. 3), while the total force exerted on the PTO axis is measured by means of a *S-beam Futek LSB302* load cell. The system is equipped with a dual-axis accelerometer (*Analog Devices ADXL203EB*) sitting on top of the prototype floater, which, together with the translational motion measurements, is explicitly used to derive rotational motion (*i.e.* angular displacement and velocity) about the fixed reference point A (see the schematic in Fig. 3). The data acquisition flow adopted comprises both host and target PCs, with the target PC directly interfaced to the WEC systems. The target PC is a Speedgoat real-time target machine (Speedgoat, 2023), which includes all the associated modules to handle I/O variables, connected via a standard Ethernet to the host PC, transferring data using a user datagram protocol (UDP). Acquisition is consistently performed at a sampling rate of 200 [Hz], for all the acquired variables, throughout the experimental campaign.

**Table 1**
Main WEC parameters.

| Parameter | Value (including units) |
|---|---|
| Floater mass | 4 [kg] |
| Mass moment of inertia w.r.t. **A** | 1 [kg m$^2$] |
| Floater draft | 0.110 [m] |
| Floater diameter at SWL | 0.256 [m] |
| Equilibrium position w.r.t. point **A** $\theta^0_{\mathbf{A}}$ | 0.523 [rad] |
| Distance points **A–C** $L_{\mathbf{AC}}$ | 0.412 [m] |
| Distance points **C–B** $L_{\mathbf{CB}}$ (in eq.) | 0.381 [m] |
| Distance points **A–B** $L_{\mathbf{AB}}$ | 0.200 [m] |
| Distance points **A–E** $L_{\mathbf{AE}}$ | 0.484 [m] |
| Distance points **A–E** in $x$ | 0.437 [m] |
| Distance points **A–E** in $z$ | 0.210 [m] |
| Centre of gravity in $x$ | 0.415 [m] |
| Centre of gravity in $z$ | −0.206 [m] |
| Centre of buoyancy in $x$ | 0.437 [m] |
| Centre of buoyancy in $z$ | −0.321 [m] |
| Arm mass | 1.157 [kg] |
| Arm moment of inertia w.r.t. **A** | 0.060 [kg m$^2$] |

From now on, we use the following convention w.r.t. the WEC prototype main variables, all of which (either by direct measurement or reconstruction/estimation) are effectively considered within the experimental campaign[2]:

(M) Measured variables:

- $z_{\text{PTO}}$: Linear displacement of the PTO motor. This can be measured either via the incorporated driver sensor, or the laser sensor on top of the PTO axis.
- $a_{\mathbf{E}}$: Linear acceleration of the WEC floater at point **E**. This can be measured by virtue of the accelerometer on top of the floater.
- $f_{\mathbf{B}}$: Force at point **B**. This can be measured directly by the load cell sitting on the PTO axis.

(E) Reconstructed/estimated variables:

- $f_\theta$: Torque (in [N m]) w.r.t. point **A**.
- $z_\theta$: Angular displacement (in [rad]) of the WEC prototype w.r.t. point **A**.
- $v_\theta$: Angular velocity (in [rad/s]) of the WEC prototype w.r.t. point **A**.
- $a_\theta$: Angular acceleration (in [rad/s$^2$]) of the WEC prototype w.r.t. point **A**.

In particular, $f_\theta$, $z_\theta$, and $a_\theta$ can be reconstructed using the set of measured variables listed above in (M), *i.e.* (see *e.g.* Ringwood et al., 2019)

$$
\begin{aligned}
f_\theta &= f_{\mathbf{B}} \cos\left(\sin^{-1}\left(\frac{L_{\mathbf{AC}}^2 - L_{\mathbf{AB}}^2 - \left(L_{\mathbf{CB}} + z_{\text{PTO}}\right)^2}{-2L_{\mathbf{AB}}^2\left(L_{\mathbf{BC}} + z_{\text{PTO}}\right)}\right)\right) L_{\mathbf{AB}}, \\
z_\theta &= \theta^0_{\mathbf{A}} - \sin^{-1}\left(\frac{\left(L_{\mathbf{CB}} + z_{\text{PTO}}\right)^2 - L_{\mathbf{AC}}^2 - L_{\mathbf{AB}}^2}{-2L_{\mathbf{AC}}L_{\mathbf{AB}}}\right), \\
a_\theta &= \frac{a_{\mathbf{E}}}{L_{\mathbf{AE}}}.
\end{aligned}
\tag{1}
$$

The only variable in (E) which cannot be directly computed via the measured quantities in (M) is the velocity of the system w.r.t. point **A**, *i.e.* $v_\theta$, requiring estimation in software. To do this with the available measures, described in the paragraph immediately above, we use a Kalman Filtering (KF) technique (see *e.g.* Chui, Chen, et al., 2017) to provide estimates of $v_\theta$ when needed. Note that the same procedure, for estimation of $v_\theta$, has been employed accordingly in *e.g.* Faedo et al. (2023) and Ringwood et al. (2019), for the same prototype device.

[2] From now on, the dependence on $t$ is dropped when clear from the context.

**Table 2**
Waves tested within the presented control-oriented experimental campaign.

| ID | Type | $T_p$ [s] | $H_s$ [m] | $\gamma$ | Length [s] |
|---|---|---|---|---|---|
| ISS1 | Irregular | 1,412 | 0,063 | 3,3 | 300 |
| ISS2 | Irregular | 1,836 | 0,104 | 3,3 | 300 |
| ISS3 | Irregular | 0,988 | 0,021 | 1 | 300 |

### 2.3. Device positioning and layout design

Three prototypes (D1 to D3) are considered and placed within the wave basin for this WEC array experimental campaign, each mounted on a gantry by means of a supporting structure (see Fig. 1). These devices are placed in a row-like formation, with a distance of 39 [cm] from centre to centre of adjacent devices. Note that this corresponds to approximately 1.5 times the diameter of the prototype floater (see Table 1), resulting in an inter-device distance (floater edge-to-edge) of approximately 1 radius, *i.e.* 13 [cm]. Each single prototype can be lifted out of the water manually, hence facilitating the testing of different layout configurations by simply pulling a specific set of devices out of the basin.

We consider 4 different layout configurations (L0 to L3) involving up to 3 different devices operating simultaneously within the basin, as schematically illustrated within Fig. 2. The choice of these layouts is, naturally, not arbitrary, as detailed in the following. We first note that the testing set is comprised of one layout with a single device (L0), two with two devices (L1 and L2), and, finally, one layout with three WECs operating within the basin (L3). L0, which, as discussed within Section 1, has been considered previously in the modelling/validation literature for this specific Wavestar prototype (see *e.g.* Heo & Koo, 2021; Ringwood et al., 2019; Tona, Sabiron, Nguyen, Mérigaud, & Ngo, 2020; Zurkinden, Ferri, Beatty, Kofoed, & Kramer, 2014 and, in particular, Faedo et al. (2023), under moment-based control conditions), is chosen as the 'baseline' case, and consists of a standard single device configuration. L1 to L2 constitute the first set of tested layouts with multiple WEC prototypes. These layouts are designed with essentially the same formation, but with different inter-device distances. The underpinning designs for L1 to L2 allows for direct characterisation of the effect of interactions between devices as a function of the distance between bodies (see *e.g.* Babarit, 2013; Chen, Gao, Meng, & Fu, 2016; De Andrés, Guanche, Meneses, Vidal, & Losada, 2014; Falcao, 2002). L3 incorporates a third device into the basin, and is designed as a natural 'extension' of L1 and L2.

### 2.4. Sea states definitions

This section discusses the definition of the tested sea state conditions selected for this experimental campaign. As it is virtually always the case within the marine/ocean engineering community, realistic waves can be represented in terms of a set of stochastic descriptions, with an associated (dense) spectrum (see *e.g.* Ochi, 1998). While different models can be used to characterise ocean waves, a particularly popular representation is that provided by the so-called JONSWAP spectrum (Hasselmann, Dunckel, & Ewing, 1980), describing wind-generated seas with fetch limitations. Within such a stochastic description, three main parameters can be identified, *i.e.* significant wave height $H_s$, peak wave period $T_p$, and peak-enhancement factor $\gamma$.

Three irregular sea states (ISS1 to ISS3) are considered within this experimental campaign, as described in Table 2. The parameters for these conditions have been directly adopted from the benchmark control case established by the WEC$^3$OMP (Ringwood et al., 2019), and aim to represent diverse operating sea states for controlled device motion conditions. The theoretical spectra (normalised w.r.t. ISS2, which is the most energetic condition) associated with these sea states are shown in Fig. 4. Two narrow-banded operating scenarios (ISS1 and

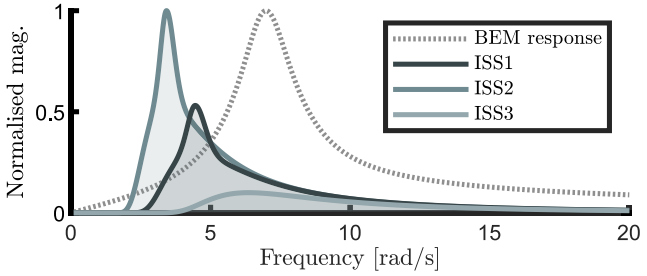


**Fig. 4.** Theoretical spectra for the irregular wave conditions used within this experimental study.

ISS2) are considered, with different peak periods and associated significant wave heights. Finally, ISS3 represents a broad-banded operating case, with significant energy content covering low-, resonance, and high-frequency components. Note that, for reference, Fig. 4 includes a characterisation of the I/O magnitude response (torque-to-velocity — see Section 3) of the single prototype system (dotted), computed numerically using boundary element methods (BEMs) (see *e.g.* Kurnia & Ducrozet, 0000).

## 3. Experimental WEC array modelling

This section introduces the modelling framework considered within this experimental campaign, inspired by the results obtained for the single device case presented in Faedo et al. (2023), now derived for farms of WEC systems. In particular, we consider the dynamical model associated with each WEC array layout considered about the reference point **A** in Fig. 3, for each device involved. To be precise, let $N \in \mathbb{N}$ be the number of devices involved in a particular array configuration. Considering the angular velocity about **A** as the system output, the I/O dynamical equation can be written in terms of a representative linear operator $G_\theta : \mathbb{C} \to \mathbb{C}^{N\times N}$, $s \mapsto G_\theta(s)$, *i.e.*

$$V_\theta(s) = G_\theta(s)\left(F_\theta(s) + U(s)\right), \tag{2}$$

where $G_\theta(s)$ is both bounded-input bounded-output (BIBO) stable and positive real, *i.e. passive* (see *e.g.* Faedo, Peña-Sanchez, Carapellese, Mattiazzo and Ringwood, 2021; Taghipour, Perez, & Moan, 2008), $v_\theta(t) \in \mathbb{R}^N$ and $f_\theta(t) \in \mathbb{R}^N$ are the angular velocity and wave excitation torque vectors about the reference point **A** (following the notation introduced in Section 2), respectively, and $u(t) \in \mathbb{R}^N$ represents the control input, to be designed such that the mechanical energy extracted from the incoming wave field is maximised, for each layout considered.

In the following, the computation of the map $G_\theta$ in (2) is addressed, based on a black-box system identification approach. The computed models, according to each tested WEC array configuration, are then subsequently considered for control design purposes, within Section 4.

### 3.1. System identification

In this study, and inspired by the single device case presented in Faedo et al. (2023), the characterisation of the map $G_\theta$ in (2) is pursued via system identification procedures. In particular, a black-box system identification method is employed (see, for instance, Ljung, 1999), with an appropriate definition of a set of I/O experiments, designed to characterise the underlying dynamics, for each WEC layout tested within this experimental campaign.

**Remark 1.** An alternative path, to that pursued within this study, would be to follow standard (white-box) physical modelling approaches, where BEM solvers are employed to compute a numerical characterisation of the device based on potential flow theory (Papillon, Costello, & Ringwood, 2020). This path is not followed within this paper since, as detailed in *e.g.* Faedo et al. (2023), such an approach only focuses on the hydrodynamics associated with the WEC array, systematically 'ignoring' any non-ideal physical characteristics associated with the experimental nature of the setup involved. In addition, models derived from data have the added advantage of being representative of the nature (particularly amplitude) of the associated signals (Davidson, Giorgi, & Ringwood, 2015), while linear BEM-based models assume infinitesimally small movement, which is challenged under controlled conditions (Windt et al., 2021).

To be precise, we define a test (torque) input set $\mathscr{F}_{\text{ID}} = \{f^p_{\text{ID}}\}_{p\in\mathbb{N}_{\tilde{N}}} \subset \mathbb{R}$, where each $f^p_{\text{ID}}$ is a linear down-chirp signal with amplitude $A_p \in \mathscr{A}_{\text{ID}} = \{A_p\}_{p\in\mathbb{N}_{\tilde{N}}} \subset \mathbb{R}^+$, designed to excite each device within the frequency set $\mathscr{W}_{\text{ID}} = [\omega_{\text{i}}, \omega_{\text{f}}] \subset \mathbb{R}^+$, with an experiment duration of $T_{\text{ID}} \in \mathbb{R}^+$. The use of a down-chirp signal, as opposed to the more 'classical' up-chirp case, is considered to minimise the effect of wall radiated waves on the experiment results (see the arguments posed in Faedo et al. (2023) and García-Violini, Peña-Sanchez, Faedo, Ferri, and Ringwood (2023)).

Based on the input set defined above, each identification test, for every WEC array involved, is performed in terms of the following procedure: In still water, *i.e.* without the presence of waves within the basin, the set $\mathscr{F}_{\text{ID}}$ is applied via the PTO system associated with the $j$th device of the considered layout *only*, producing an associated set of angular velocity outputs $\mathscr{V}_{\text{ID}-j} = \{v^p_{\text{ID}-j}\}_{p\in\mathbb{N}_{\tilde{N}}} \subset \mathbb{R}^N$. With this information, and by consistently performing this test for each device in the layout, *i.e.* for $j \in \mathbb{N}_N$, a non-parametric frequency-domain characterisation can be readily computed in terms of the so-called average empirical transfer function estimate (aETFE) (Ljung, 1999):

$$\bar{G}_\theta(j\omega) = \begin{bmatrix}\bar{G}_{\theta_1}(j\omega) & \dots & \bar{G}_{\theta_N}(j\omega)\end{bmatrix} \in \mathbb{C}^{N\times N} \tag{3}$$

where each $\bar{G}_{\theta_j}(j\omega) \in \mathbb{C}^N$ is computed according to all $j$th tests, *i.e.*

$$\begin{aligned}\bar{G}_{\theta_j}(j\omega) &= \frac{1}{\tilde{N}}\sum_{p\in\mathbb{N}_{\tilde{N}}} \tilde{G}^p_{\theta_j}(j\omega).\\ \tilde{G}^p_{\theta_j}(j\omega) &= V^p_{\text{ID}-j}(j\omega) \oslash \left(\mathbb{1}_N \otimes F^N_{\text{ID}}(j\omega)\right),\end{aligned} \tag{4}$$

and $\tilde{G}^p_{\theta_j}(j\omega) \in \mathbb{C}^N$ in (4) represents a single ETFE associated with the input chirp amplitude $A_p$.

With the computation of $\bar{G}_{\theta_j}(j\omega)$ in (3), standard system identification techniques can be considered for parametric approximation of the corresponding response operator. In particular, within this study, we leverage frequency-domain subspace-based techniques, as per (McKelvey, Akçay, & Ljung, 1996). These non-iterative identification methods are essentially based on the extraction of a low-dimensional subspace characterising the underlying system by means of a truncated singular value decomposition of the associated input/output data. This process provides, for each considered WEC array layout, a continuous-time, finite-dimensional, strictly proper, state–space system[3]

$$G_\theta \approx G_{\text{ID}-\theta} \equiv \begin{cases}\dot{x} = Ax + B(f_\theta + u),\\ v_\theta = Cx,\end{cases} \tag{5}$$

where the triple $(A, B, C) \in \mathbb{R}^{n\times n} \times \mathbb{R}^{n\times N} \times \mathbb{R}^{N\times n}$ is minimal, and $\lambda(A) \subset \mathbb{C}_{<0}$, *i.e.* system (5) is asymptotically stable.

To illustrate the procedure described within this section, and avoid overflowing this paper with what can be considered to be analogous results, we present an appraisal of the model computed for the most 'complex' layout, *i.e.* L3, which is composed of three WEC devices aligned with respect to the $y$-axis of the basin. The set of chirp amplitudes is chosen as $\mathscr{A}_{\text{ID}} = \{2, 2.5, 3, 3.5, 4\}$ [N m], with an exciting band of $\mathscr{W}_{\text{ID}} \approx [0.1, 30]$ [rad/s], and a time-domain length set to $T_{\text{ID}} = 140$ [s]. In

[3] From now on, the dependence on $t$ is dropped when clear from the context.

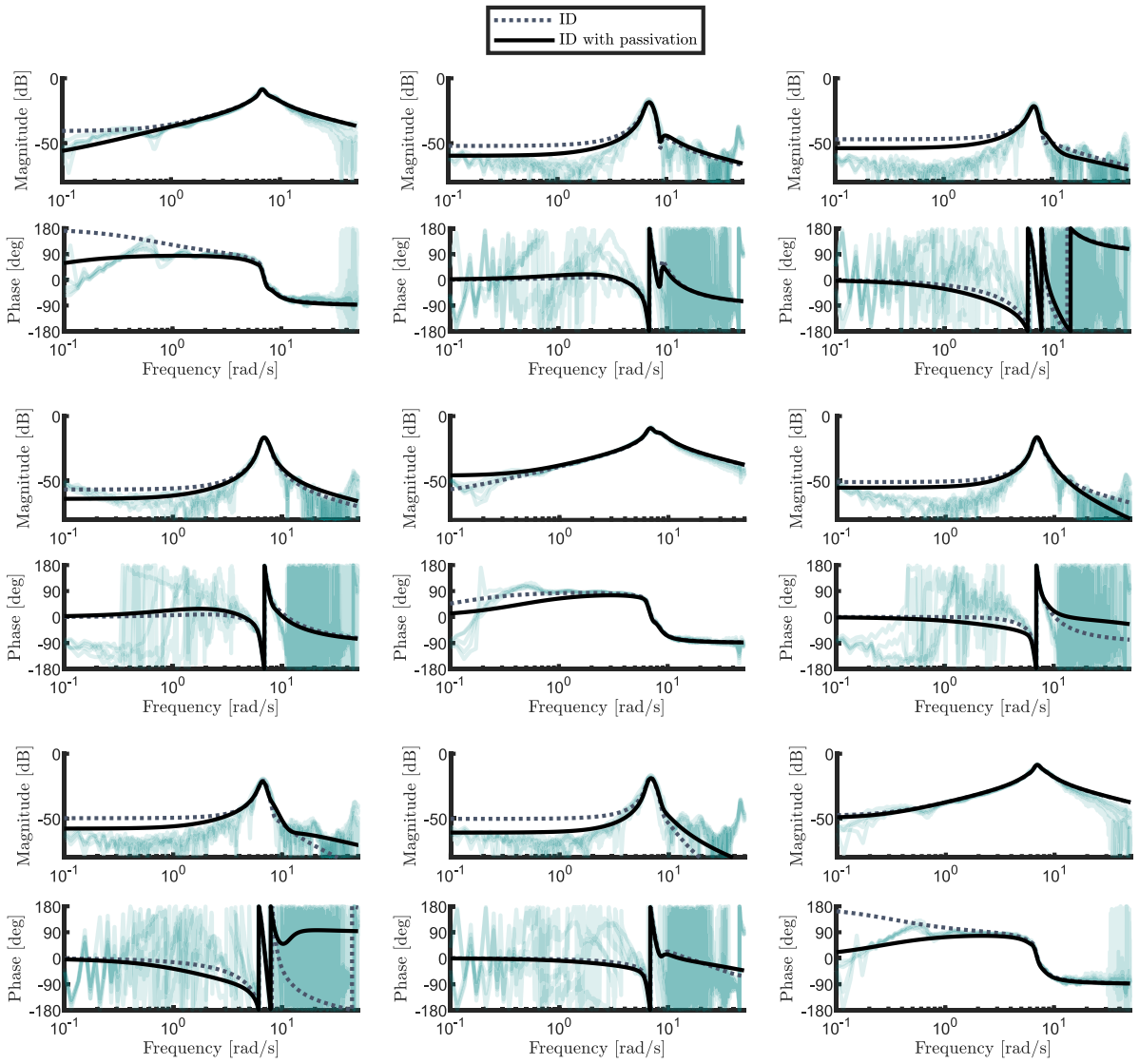


**Fig. 5.** Bode plot associated with each single ETFE, computed in terms of each performed experiment (green lines with transparency), and the response characterising the identified model $G_{\mathrm{ID}-\theta}$, without (dotted grey lines) and with (solid black lines) passivation applied. (For interpretation of the references to colour in this figure legend, the reader is referred to the web version of this article.)

particular, Fig. 5 shows the Bode plot associated with each single ETFE, computed in terms of each performed experiment (green lines with transparency), and the response characterising the identified model $G_{\mathrm{ID}-\theta}$ (dotted grey lines). Note that a significant interaction exists between WECs (especially for adjacent devices) close to the resonance condition.

### 3.2. Model passivation

Though effectively able to represent the empirical response obtained via the designed I/O experiments, the model computed in (5) does not necessarily respect the well-known positive-real condition for the map $G_\theta$ in (2). This condition, which is fundamental to guarantee the existence and uniqueness of energy-maximising solutions within moment-based theory (see Section 4.1), needs to be enforced accordingly, in order to ensure physical representativity of the computed WEC array model, for each layout considered.

To achieve this, we consider the passivised mechanism proposed in Faedo, Peña-Sanchez et al. (2021), which is based upon insertion of a suitably defined additive perturbation $\Delta C \in \mathbb{R}^{N\times n}$ to the output matrix $C$ in (5). In other words, system (5) is modified accordingly as

$$G_{\mathrm{ID}-\theta} \mapsto \begin{cases} \dot{x} = Ax + B(f_\theta + u), \\ v_\theta = (C + \Delta C)x = \widetilde{C}x, \end{cases} \tag{6}$$

where, with some abuse of notation, we keep the same variable $G_{\mathrm{ID}-\theta}$ for convenience of exposition. The value for $\Delta C$ is computed based on a linear matrix inequality (LMI) approach, where the well-known positive real lemma (Marquez, 2003, Chapter 8) is enforced, while minimising $\|\Delta C\|$ in terms of a suitable norm. The interested reader is referred to Faedo, Peña-Sanchez et al. (2021) for further detail on the underlying framework for LMI-based passivation, with the corresponding numerical implementation in Faedo (2021).

The frequency response associated with the passivated model is shown in Fig. 5, using solid black lines. Note that, while the behaviour between models (5) and (6) is similar close to resonance conditions, the low-frequency behaviour is effectively different, even for the (dominant) diagonal elements of the frequency response matrix. To further illustrate the nature of this phenomenon, analogously to Faedo, Peña-Sanchez et al. (2021), we define the following real-valued operator $\mathcal{P} : \mathbb{R} \to \mathbb{R}$

$$\mathcal{P}(\omega) = \lambda_{\min}\left(\mathscr{H}\left(G_{\mathrm{ID}-\theta}(\jmath\omega)\right)\right), \tag{7}$$

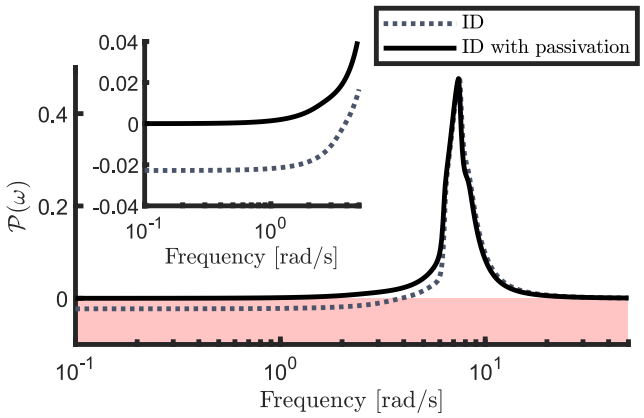


**Fig. 6.** Output map $\mathcal{P}$ for non-passivised (dotted grey) and passivised (solid black) identified models. The red colour is used to indicate the area of violation of the positive real condition. (For interpretation of the references to colour in this figure legend, the reader is referred to the web version of this article.)

which essentially measures the minimum eigenvalue $\lambda_{\min}$ associated with the Hermitian matrix $\mathscr{H}(G_{\mathrm{ID}-\theta}(j\omega))$. In other words, if $\mathcal{P}(\omega) \in \mathbb{R}^{+}$ for every $\omega$, then the associated system $G_{\mathrm{ID}-\theta}$ is positive real. Based on the definition provided in (7), Fig. 6 illustrates the output of $\mathcal{P}$ for the identified model (dotted grey), and identified model with passivation (solid black), *i.e.* Eqs. (5) and (6), respectively. Note that, the non-passivised model (5) presents negative values of $\mathcal{P}$, particularly within the low-frequency range. In contrast, the passivised model (6), by virtue of a suitable design of $\Delta C$, provides a response consistent with a positive real system, while still preserving an accurate representation of the ETFE computed (see Fig. 5).

### 3.3. Model assessment

Within this section, we provide an assessment of the models computed via the process described in Sections 3.1 and 3.2. To achieve such an objective, a measurement of the wave excitation force $f_\theta$, and corresponding angular velocity output $v_\theta$, are required, in order to assess the quality of the identified system, for each generated wave within the basin and WEC array layout tested. This is achieved, within the wave tank, in terms of a 'two-stage' process, as described in the following.

In the first stage, the devices involved in each layout are essentially locked in position (each associated PTO motor shaft is locked — see *e.g.* Faedo et al., 2023), and hence the force $f_{\mathbf{B}}$ exerted by each particular wave realisation can be measured directly via the load cell attached to point **B** (see Section 2.2 and Fig. 3), and transformed to torque w.r.t. point **A**, *i.e.* $f_\theta$, via Eq. (1). To illustrate this first stage, Fig. 7 shows a time-snippet of the measured wave excitation force for ISS1, in the case of L3 (D1 to D3).

In the second stage, and by generating the same wave realisations within the basin, two main motion variables are measured directly, for each corresponding WEC array layout involved, using the instrumentation available on each device: Linear (PTO) position $z_{\mathrm{PTO}}$ (either via the incorporated sensor within the corresponding driver or the laser position sensor situated on top of the motor — see Section 2.2), and floater (linear) acceleration $\ddot{z}_{\mathbf{E}}$ (measured via the accelerometer placed on top of each floater). These two variables can be used to provide estimates of $v_\theta$, by means of a standard Kalman Filter (see the discussion provided in Section 2.2).

Following the acquisition procedure described above, we proceed to provide a numerical appraisal of the performance of the computed models for each WEC array layout considered, and sea state condition generated within the basin. To begin the analysis, and illustrate performance in graphical terms, *i.e.* qualitatively, Fig. 8 shows measured

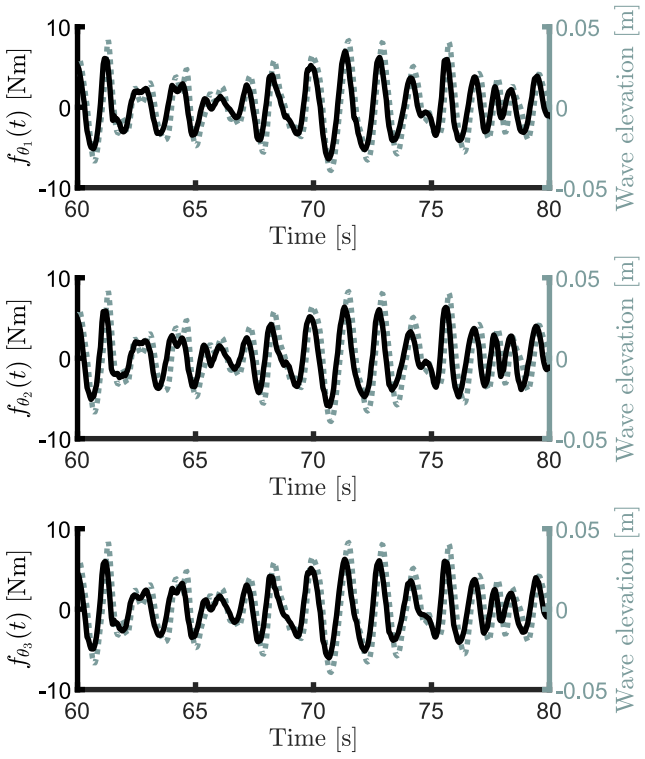


**Fig. 7.** Left axis: Time-snippet of the measured wave excitation force for ISS1, for the case of L3 (D1 to D3). Right axis: Corresponding time-snippet for free-surface elevation, as measured by wave probes 1, 2 and 3 in empty basin conditions, respectively.

(dashed grey) and passivised model (solid black) velocity outputs, for all three wave excitation forces corresponding with ISS1 (see Fig. 7), in the case of the L3 array (D1 to D3). Note that a good agreement can be appreciated between all signals, with the model effectively able to capture the main dynamics characterising the WEC array.

Finally, and to provide a quantitative measure of performance for the computed models, we define the normalised mean absolute percentage error (NMAPE) as

$$\mathrm{NMAPE}(f, f_{\mathrm{ref}}) = \frac{100}{N_f} \sum_{i=1}^{N_f} \frac{|f(t_i) - f_{\mathrm{ref}}(t_i)|}{\max_i(|f_{\mathrm{ref}}(t_i)|)}\%, \tag{8}$$

where $N_f \in \mathbb{N}$ refers to the number of samples associated with the (sampled) signal $f(t) \in \mathbb{R}$, and where $f_{\mathrm{ref}}(t)$ is the target (reference) signal. Based on the definition provided in (8), Table 3 reports the NMAPE value for all the layouts considered, in every individual wave condition. Note that both the individual and mean errors are always below 10%, showing the capabilities of each model to represent all the considered layouts, for each operating condition tested within the basin.

## 4. Controller design

Within this section, we describe the overall control loop and solution employed for the experimental campaign, for each WEC array layout and sea state considered. As discussed in Section 1, the controller considered, termed SM$^2$C, can be seen as a 'composite' system, with two main stages. First, a model-based optimal reference generation algorithm is employed, based on the theory of moments and steady-state response properties associated with the WEC array under analysis (see Faedo, Scarciotti et al., 2019; Faedo et al., 2021a and Section 4.1). This stage produces a set of desired signals $\{u_\theta^{\mathrm{opt}}, z_\theta^{\mathrm{opt}}, v_\theta^{\mathrm{opt}}\}$, describing optimal torque, angular displacement, and angular velocity, which produce maximum energy absorption from the incoming wave, according

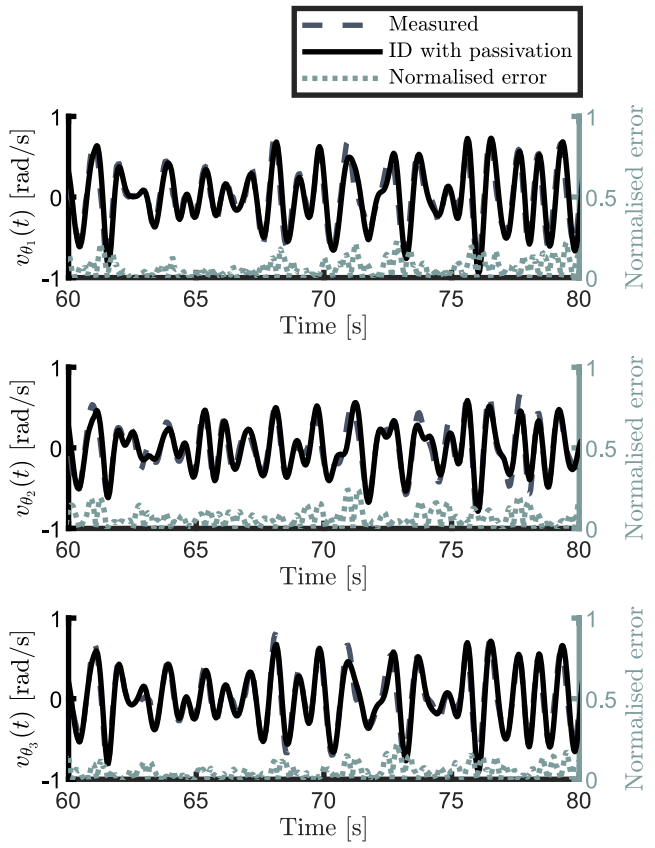


**Fig. 8.** Left axis: Measured (dashed grey) and passivised model (solid black) outputs (angular velocity), for all three wave excitation forces corresponding with ISS1, in the case of L3 (D1 to D3). Right axis: Corresponding instantaneous normalised error (in accordance with the definition in (8)).

**Table 3**
NMAPE for each identified (and passivised) model, corresponding to layouts L0, L1, L2 and L3, and every tested sea state.

| Layout | ID | D1 | D2 | D3 | Mean |
|---|---|---|---|---|---|
| *L0* | ISS1 | 7.10% | – | – | 7.10% |
| | ISS2 | 6.42% | – | – | 6.42% |
| | ISS3 | 6.32% | – | – | 6.32% |
| *L1* | ISS1 | 4.50% | 4.09% | – | 4.30% |
| | ISS2 | 5.88% | 6.07% | – | 5.98% |
| | ISS3 | 6.21% | 4.12% | – | 5.17% |
| *L2* | ISS1 | 8.78% | – | 5.83% | 7.31% |
| | ISS2 | 6.81% | – | 5.56% | 6.20% |
| | ISS3 | 6.77% | – | 6.24% | 6.51% |
| *L3* | ISS1 | 6.19% | 6.58% | 4.61% | 5.80% |
| | ISS2 | 5.82% | 6.55% | 5.16% | 5.85% |
| | ISS3 | 6.70% | 6.60% | 7.08% | 6.87% |

to the current operational sea state. These optimal target profiles are produced in a receding-horizon fashion, exploiting knowledge of the wave excitation force $f_\theta$ in a pre-defined time window (see Section 4.1). Following optimal reference generation, the second stage is essentially composed of an inner tracking loop which, exploiting variable structure systems (sliding mode, in this case) theory, achieves robust following of the computed energy-maximising profiles, hence guaranteeing optimal operation of each WEC layout and sea-state considered within this experimental campaign. An overall view of the control loop is presented in Fig. 9, schematically designed for the most 'complex' array case, *i.e.* L3, with all three devices within the basin.

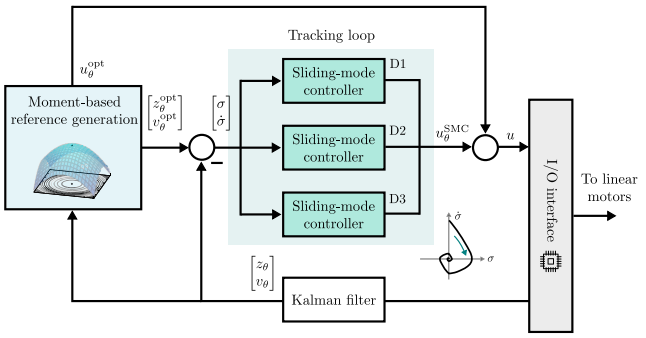


**Fig. 9.** Schematic of the composite loop for the SM$^2$C, in the case of L3.

### 4.1. Optimal reference generation via moment-based theory

Reference generation is based on providing a solution to the energy-maximising optimal control problem (OCP) for WEC systems, adopting a receding-horizon approach. To be precise, absorbed power is set as the main objective function $\mathscr{J}_K$ in this study, *i.e.*

$$\mathscr{J}_K \mapsto -\frac{1}{T_\mathrm{h}} \int_{\Xi_K} v_\theta^\mathsf{T}\, u \,\mathrm{d}t, \tag{9}$$

where $\Xi_K = [K\Delta_\mathrm{h}, K\Delta_\mathrm{h} + T_\mathrm{h}] \subset \mathbb{R}^+$, $K \in \mathbb{N}$, where $T_\mathrm{h}$ denotes the length of the $K$th time-window, *i.e.* the time horizon, in which (9) is effectively maximised, and where $\Delta_\mathrm{h}$ denotes the receding time step. In this paper, and aiming to guarantee the safe operation of all the devices involved in any given array configuration, we consider a set of input constraints $\mathscr{C}$ along with $\mathscr{J}_K$ for the effective definition of the associated OCP. In particular,

$$\mathscr{C} = \left\{ u \in \mathbb{R}^N \;\middle|\; |u| \leq U_\mathrm{max} \right\},\ t \in \mathbb{R}^+, \tag{10}$$

where $U_\mathrm{max} \in \mathbb{R}^N$ denotes the maximum admissible value for the control torque. With the objective function (9), and the set of constraints in (10), the energy-maximising OCP for WEC systems ($\mathrm{P}_K$), giving origin to the optimal reference generation procedure, can be stated as:

$$\begin{aligned} (\mathrm{P}_K) : \left\{ u_\theta^\mathrm{opt}, z_\theta^\mathrm{opt}, v_\theta^\mathrm{opt} \right\} \leftarrow\!\shortmid & \max_{u, z_\theta, v_\theta} \mathscr{J}_K \\ & \text{subject to:} \\ & \text{Array dynamics } G_{\mathrm{ID}-\theta}(6). \\ & \text{Constraint set } \mathscr{C} \text{ in (10).} \end{aligned} \tag{11}$$

A summary of the receding-horizon reference generation procedure can be then synthesised in the following steps:

**(1)** $\mathscr{R}_K : \left\{ u_\theta^\mathrm{opt}, z_\theta^\mathrm{opt}, v_\theta^\mathrm{opt} \right\} \leftarrow\!\shortmid$ Solve $(\mathrm{P}_K)$ for the time window $\Xi_K$.

**(2)** Provide a reference set $\mathscr{R}_K$ for the inner tracking loop in the interval $[K\Delta_\mathrm{h}, (K+1)\Delta_\mathrm{h}] \subset \mathbb{R}^+$, *i.e.* for a single receding horizon step $\Delta_h$.

**(3)** Move $\Xi_K \mapsto \Xi_{K+1}$ and go back to **(1)**.

Clearly, Problem $(\mathrm{P}_K)$, as in (11), is defined over an infinite-dimensional space. In order to provide a computationally tractable approximation of Problem $(\mathrm{P}_K)$, *i.e.* implementable in real-time, we leverage the direct optimal control procedure for WECs based on the theory of moments. Moment-based theory, originally developed within the field of model order reduction for ordinary differential equations (Astolfi et al., 2020), has been exploited for direct transcription of optimal control problems for the first time in Faedo, Scarciotti, Astolfi, and Ringwood (2018), showing that this mathematical framework is able to produce a numerically tractable nonlinear program (NP), later solved using state-of-the-art optimisation routines. Several variations of this algorithm have been developed, including *e.g.* nonlinear (Faedo, Giorgi, Ringwood and Mattiazzo, 2022; Faedo, Scarciotti, Astolfi, &

Ringwood, 2021b) and robust (Faedo, García-Violini, Scarciotti, Astolfi and Ringwood, 2019) solutions, with a corresponding extension to WEC arrays in Faedo et al. (2021a).

**Remark 2.** Note that, in order to compute the associated optimal trajectories resulting from (11), knowledge of the wave excitation force is required within each window $\Xi_K$, *i.e.* the optimal control action is effectively non-causal, in line with standard energy-maximising theory for WECs (see *e.g.* Ringwood, Zhan, & Faedo, 2023). Given that the main objective of this paper is the development, design, experimental implementation, and performance appraisal of the SM$^2$C for WEC array systems (the subject of this section) and the corresponding implementation presented in Section 5, knowledge of the wave excitation force, for each time window $\Xi_K$, is leveraged by following the procedure described in Section 3.3, for each sea state and array layout involved. This is performed to decouple estimation/forecasting and control problems (which is the main focus of this study), respectively, in the spirit of the separation principle. Nonetheless, we stress that, if required, wave excitation force estimates (instantaneous and future values) can be directly incorporated in the moment-based reference generation procedure. As a matter of fact, this has been considered explicitly, in combination with moment-based theory, in the recent study (Faedo et al., 2023), where a single WEC device is considered under optimal control conditions.

Within the following paragraphs, and aiming to keep this paper reasonably self-contained, we recall the main concepts underlying moment-based theory for arrays of WEC systems, in a centralised fashion. In particular, the main steps taken for the direct transcription of Problem ($\mathrm{P}_K$), in terms of moments, are both elucidated and detailed, in order to provide the corresponding optimal reference profiles to be tracked by the inner sliding mode controller, described in Section 4.2.

To be precise, for any given WEC array layout with $N$ devices, let $f_\theta$ be described in terms of the following autonomous, continuous-time, multiple-output, signal generator $\mathscr{G}$, *i.e.*

$$\mathscr{G}:\begin{cases}\dot{Z}=\left(\mathbb{I}_N\otimes S\right)Z,\\ f_\theta=L_\theta Z,\\ S=\bigoplus_{p=1}^{\nu/2}\begin{bmatrix}0 & p\omega_0\\ -p\omega_0 & 0\end{bmatrix},\\ Z^0=Z(K\Delta_{\mathrm{h}}),\end{cases}\tag{12}$$

where the triple $(\mathbb{I}_N\otimes S, L_\theta, Z^0)\in\mathbb{R}^{N\nu\times N\nu}\times\mathbb{R}^{N\times N\nu}\times\mathbb{R}^{N\nu\times N}$ is minimal, *i.e.* the pairs $(\mathbb{I}_N\otimes S, L_\theta)$ and $(\mathbb{I}_N\otimes S, Z^0)$ are observable and reachable, respectively. Furthermore, note that $\lambda(S)=\{\pm p\jmath\omega\}_{p\in\mathbb{N}_\nu}\subset\mathbb{C}^0$ so that it is straightforward to show that the output of (12) is always bounded and $T_{\mathrm{h}}$-periodic, with $T_{\mathrm{h}}=2\pi/\omega_0$.

With the representation of $f_\theta$ as in (12), and following the arguments in *e.g.* Faedo, Giorgi et al. (2022) and Faedo et al. (2021b), we proceed to represent the control input in terms of the so-called *extended* signal generator $\widetilde{\mathscr{G}}$, *i.e.*

$$\widetilde{\mathscr{G}}:\begin{cases}\dot{\widetilde{Z}}=\left(\mathbb{I}_N\otimes\widetilde{S}\right)\widetilde{Z},\\ f_\theta=\widetilde{L_\theta}\widetilde{Z},\\ u=\widetilde{L_u}\widetilde{Z},\\ \widetilde{S}=S\oplus\left(\bigoplus_{p=\nu+1}^{\iota/2}\begin{bmatrix}0 & p\omega_0\\ -p\omega_0 & 0\end{bmatrix}\right),\\ \widetilde{L_\theta}=\begin{bmatrix}L_\theta & 0\end{bmatrix},\\ \widetilde{Z}^0=\begin{bmatrix}Z^0 & \widetilde{Z}(K\Delta_{\mathrm{h}})\end{bmatrix},\end{cases}\tag{13}$$

with $\tilde{\nu}=\nu+\iota$, and where the pair $(\mathbb{I}_N\otimes\widetilde{S},\widetilde{Z}^0)\in\mathbb{R}^{N\tilde{\nu}\times N\tilde{\nu}}\times\mathbb{R}^{N\tilde{\nu}\times N}$ is reachable.

**Remark 3.** Note that the wave excitation force $f_\theta$, as defined in $\mathscr{G}$, is written in terms of the extended generator $\widetilde{\mathscr{G}}$ by merely using an inclusion operator, *i.e.* $\mathbb{R}^{N\nu\times N}\hookrightarrow\mathbb{R}^{N\tilde{\nu}\times N}:L_\theta\hookrightarrow\widetilde{L_\theta}=[L_\theta\ 0]$.

**Remark 4.** The signal generator $\widetilde{\mathscr{G}}$ in (13) is an extension of $\mathscr{G}$ in (12) in the sense that it incorporates $\iota/2$ additional harmonics of the fundamental frequency $\omega_0$ to represent, in implicit form, the control input $u$. In other words, given the excitability of the pair $(\mathbb{I}_N\otimes\widetilde{S},\widetilde{Z}^0)$, and the nature of the eigenspace of $\widetilde{S}$, it is relatively straightforward to show that, according to (13),

$$u_i\in\operatorname{span}\left(\{\cos(p\omega_0 t),\sin(p\omega_0 t)\}_{p\in\mathbb{N}_{\tilde{\nu}}}\right),\tag{14}$$

for every $i\in\mathbb{N}_N$.

With the definition of the signal generator in (13), and the identified passive system (6), it is possible to show that there exists a unique (Faedo et al., 2021a) matrix $\Pi$ which solves the Sylvester equation

$$A\Pi+B\left(\widetilde{L_\theta}-\widetilde{L_u}\right)=\Pi\left(\mathbb{I}_N\otimes\widetilde{S}\right),\tag{15}$$

and, for any given trajectory $\widetilde{Z}(t)$ of $\widetilde{\mathscr{G}}$, fully characterises the steady-state response $x_{\mathrm{ss}}$ of (6), *i.e.* $x_{\mathrm{ss}}(t)=\Pi\widetilde{Z}(t)$.

**Remark 5.** Note that, correspondingly, the steady-state *output* response can be written in terms of the unique solution of (15) as $v_{\theta_{\mathrm{ss}}}=\widetilde{C}\Pi\widetilde{Z}(t)=\widetilde{L_v}\widetilde{Z}(t)$, with $\widetilde{L_v}\in\mathbb{R}^{N\times N\tilde{\nu}}$. Following standard notation, the matrix $\widetilde{L_v}$ is termed the *moment* of system (6) at the extended signal generator (13).

As per the framework presented in Faedo et al. (2021a), the solution of (15) can be computed explicitly, by leveraging the vectorisation operator, *i.e.*

$$\begin{aligned}\operatorname{vec}\left(\widetilde{L_v}\right)&=\left(\mathbb{I}_{\tilde{\nu}}\otimes\widetilde{\Psi}\right)\operatorname{vec}\left(\widetilde{L_\theta}-\widetilde{L_u}\right),\\ \widetilde{\Psi}&=\left(\mathbb{I}_{\tilde{\nu}}\otimes C\right)\widetilde{\Phi}^{-1}\left(\mathbb{I}_{\tilde{\nu}}\otimes B\right),\\ \widetilde{\Phi}&=\widetilde{S}\otimes\mathbb{I}_n+\mathbb{I}_{\tilde{\nu}}\otimes A,\end{aligned}\tag{16}$$

where $0\notin\lambda(\Phi)$ since $\lambda(\widetilde{S})\cap\lambda(A)=\emptyset$ (see *e.g.* Astolfi, 2010; Brewer, 1978). The moment-based representation arising from the implicit form signal generator (13), and corresponding moment equation (16), can be used to transcribe the OCP (11) into a finite-dimensional NP (see Faedo, Scarciotti et al., 2019; Faedo et al., 2021a for further detail),

$$\begin{aligned}&\widetilde{(\mathrm{P}_K)}:\\ &u^{\mathrm{opt}}=\widetilde{L_u}^{\mathrm{opt}}\widetilde{Z},\\ &z_\theta^{\mathrm{opt}}=\left(\mathbb{I}_{\tilde{\nu}}\otimes\widetilde{\Psi}\right)\operatorname{vec}\left(\widetilde{L_\theta}-\widetilde{L_u}^{\mathrm{opt}}\right)\left(\mathbb{I}_N\otimes\widetilde{S}^{-1}\right)\widetilde{Z},\\ &v_\theta^{\mathrm{opt}}=\left(\mathbb{I}_{\tilde{\nu}}\otimes\widetilde{\Psi}\right)\operatorname{vec}\left(\widetilde{L_\theta}-\widetilde{L_u}^{\mathrm{opt}}\right)\widetilde{Z},\end{aligned}\tag{17}$$

with the optimal moment-based representation $\widetilde{L_u}^{\mathrm{opt}}$ the solution of the *strictly concave* QP

$$\begin{aligned}\widetilde{L_u}^{\mathrm{opt}}=\arg\max_{\widetilde{L_u}\in\mathbb{R}^{N\times N\tilde{\nu}}}\ &\frac{1}{2}\operatorname{vec}\left(\widetilde{L_u}\right)^{\mathsf{T}}\left(\mathbb{I}_{\tilde{\nu}}\otimes\widetilde{\Psi}^{\mathsf{T}}\right)\operatorname{vec}\left(\widetilde{L_u}\right)\\ &-\frac{1}{2}\operatorname{vec}\left(\widetilde{L_\theta}\right)^{\mathsf{T}}\left(\mathbb{I}_{\tilde{\nu}}\otimes\widetilde{\Psi}^{\mathsf{T}}\right)\operatorname{vec}\left(\widetilde{L_u}\right),\\ \text{subject to:}\\ \widetilde{L_u}Z\in\mathscr{C},\ &\forall t\in\widetilde{\mathcal{T}}=\{t_i\}_{i\in\mathbb{N}_{N_c}},\end{aligned}\tag{18}$$

and where the finite-dimensional set $\widetilde{\mathcal{T}}$ is used to collocate (uniformly) the set of constraints in (10) at $N_c\in\mathbb{N}$ time instants. In particular, via collocation and moment-based variables, note that the set $\mathscr{C}$ in (10) can be mapped to a closed half-space $\mathscr{L}_u$ accordingly, *i.e.*

$$\widetilde{L_u}Z\in\mathscr{C}\xrightarrow{t\in\widetilde{\mathcal{T}}}\widetilde{L_u}\in\mathscr{L}_u\subset\mathbb{R}^{N\times N\tilde{\nu}},\tag{19}$$

with

$$\begin{aligned}
&\mathscr{L}_u = \left\{ \widetilde{L_u} \in \mathbb{R}^{N\times N\tilde{\nu}} \;\middle|\; \mathcal{A}_u \mathrm{vec}\left(\widetilde{L_u}\right) \leq \mathcal{B}_u \right\},\\
&\mathcal{A}_u = \Delta,\\
&\mathcal{B}_u = U_{\max}\mathbb{1}_{2NN_c},\\
&\Delta = \begin{bmatrix} \Lambda^{\mathsf{T}} & -\Lambda^{\mathsf{T}} \end{bmatrix}^{\mathsf{T}},\\
&\Lambda = \begin{bmatrix} \widetilde{Z}(t_1) & \dots & \widetilde{Z}(t_{N_c}) \end{bmatrix}^{\mathsf{T}},
\end{aligned} \tag{20}$$

so that (18) can be solved using efficient QP numerical solvers (see *e.g.* Boyd & Vandenberghe, 2004), and hence the optimal reference variables in (17) can be computed in polynomial time (Vavasis, 2001).

**Remark 6** (*Strict*)**.** concavity of Problem $\widetilde{(\mathrm{P}_K)}$ and, hence, the uniqueness of solutions for the NP in (18), can be linked to the nature of the matrix $\widetilde{\Psi}$ in Eq. (16). In particular, (18) has a unique (well-defined) solution if and only if $\mathscr{H}(\widetilde{\Psi})$ is positive-definite, which is always guaranteed if the WEC array system (6) is passive (Faedo et al., 2021a). Note that this is effectively the case within this study, due to the application of the passivation procedure described within Section 3.2, and hence Problem $\widetilde{(\mathrm{P}_K)}$ is consistently well-defined.

While the $T_{\mathrm{h}}$-periodicity assumption for $f_\theta$, arising from the implicit form representation in (13), has been shown to be valid for sufficiently large $T_{\mathrm{h}}$ in numerous studies (see *e.g.* Mérigaud & Ringwood, 2017), within the receding-horizon OCP formulation presented in (11) the length of the time-window is commonly chosen following a rather conservative approach, to keep the computational requirements associated with solving (18) within real-time limits. This, in turn, naturally creates an issue when attempting to represent $f_\theta$ in implicit form (13). We address this issue in the following paragraphs, based on the framework proposed in Faedo, Peña-Sanchez et al. (2020).

Let the current time window $\Xi_K$ (as per (11)), be defined in terms of the following relation

$$\Xi_K = \left[K\Delta_{\mathrm{h}}, t_K^{\mathrm{m}}\right] \cup \left(t_K^{\mathrm{m}}, K\Delta_{\mathrm{h}} + T_{\mathrm{h}}\right], \tag{21}$$

where $t_K^{\mathrm{m}}$ denotes the current time instant, located, without any loss of generality, at the centre point of $\Xi_K$. Within this set, we defined the so-called apodised (*i.e.* windowed) wave excitation force $f_\theta^\vartheta$ as

$$f_\theta^\vartheta = f_\theta \odot \left(\mathbb{1}_N \otimes \vartheta\right), \ \forall t \in \Xi_K, \tag{22}$$

where the map $\vartheta : \Xi_K \to [0, 1]$ is used to smoothly drive $f_\theta$ to zero at the edges of the set $\Xi_K$, so that the derivative of its corresponding $T_{\mathrm{h}}$-periodic extension is sufficiently smooth (Prabhu, 2013). Fig. 10 illustrates the process defined via (22), *i.e.* the map $f_\theta \mapsto f_\theta^\vartheta$, where the function $\vartheta$ is chosen in terms of the Planck-Taper function (McKechan, Robinson, & Sathyaprakash, 2010), which optimally preserves the power spectrum of $f_\theta$ within $\Xi_K$.

Finally, following Faedo, Peña-Sanchez et al. (2020), $f_\theta^\vartheta$ can be (approximately) brought to the implicit form (13) by orthogonal projection on the set spanned by $\{Z_i\}_{i\in\mathbb{N}_{\tilde{\nu}}}$, *i.e.*

$$\widetilde{L_\theta} \simeq \begin{bmatrix} \dfrac{\langle f_\theta^\vartheta, \widetilde{Z}_1\rangle_{\Xi_K}}{\langle \widetilde{Z}_1\rangle^2_{\Xi_K}} & \dots & \dfrac{\langle f_\theta^\vartheta, \widetilde{Z}_{\tilde{\nu}}\rangle_{\Xi_K}}{\langle \widetilde{Z}_{\tilde{\nu}}\rangle^2_{\Xi_K}} \end{bmatrix}, \tag{23}$$

to subsequently solve $\widetilde{(\mathrm{P}_K)}$ in terms of (18) accordingly.

### 4.2. Tracking control via sliding modes

To guarantee operation within the conditions computed via the optimal moment-based algorithm posed in Section 4.1, within the overall SM$^2$C strategy, the optimal trajectories $u_\theta^{\mathrm{opt}}$, $z_\theta^{\mathrm{opt}}$, and $v_\theta^{\mathrm{opt}}$ are fed to an inner tracking controller, in charge of driving the system towards the designed conditions even in the presence of uncertainty, *i.e.* robustly. To achieve this, we consider a proportional–integral–derivative-like

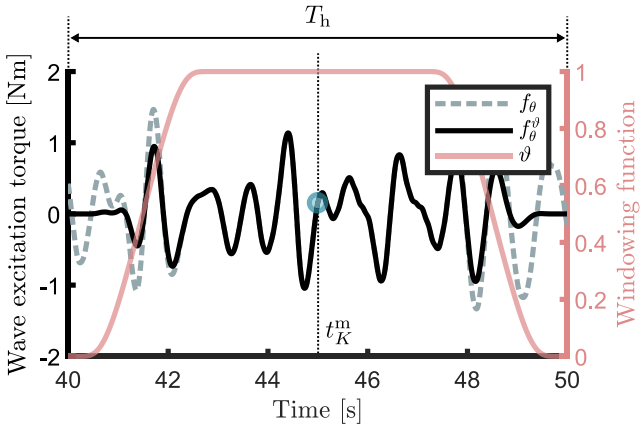


**Fig. 10.** Graphical appraisal of the windowing $f_\theta \mapsto f_\theta^\vartheta$.

*continuous* sliding mode controller (PID-SMC), as developed and proposed in Pérez-Ventura et al. (2021). In particular, we consider that the final control torque applied to the system can be decomposed as

$$u = u_\theta^{\mathrm{opt}} + u_\theta^{\mathrm{SMC}}, \tag{24}$$

where $u_\theta^{\mathrm{opt}}$ is computed in terms of the solution of (18), and $u_\theta^{\mathrm{SMC}}(t) \in \mathbb{R}^N$ denotes the contribution of the PID-like sliding mode controller.

**Remark 7.** The value associated with the moment-based solution, $u_\theta^{\mathrm{opt}}$, is effectively used in (24) to 'inform' the sliding mode controller on the optimal (ideal - *i.e.* without the presence of uncertainty) control trajectory, so as to effectively reduce the effort required by the PID-SMC to achieve the corresponding motion tracking. Note that this is analogous to the concept of the so-called 'equivalent control' in standard sliding mode theory (Utkin, 2013).

In particular, the PID-SMC is defined in terms of the two following key variables:

$$\begin{aligned}
\sigma_j &= z_j - z_{\theta_j}^{\mathrm{opt}},\\
\dot{\sigma}_j &= v_j - v_{\theta_j}^{\mathrm{opt}},
\end{aligned} \tag{25}$$

which effectively describes the error between desired and actual operation regime (*i.e.* optimal position and velocity) for the $j$-device composing the WEC array under analysis, with $j \in \mathbb{N}_N$. Furthermore, let us define the following dynamical system $e_j^\sigma$ in terms of (25):

$$e_j^\sigma : \begin{cases} \dot{m}_{j1} = m_{j2}, \\ \dot{m}_{j2} = \bar{f}_j + u_{\theta_j}^{\mathrm{opt}} + u_{\theta_j}^{\mathrm{SMC}}, \end{cases} \tag{26}$$

with $m_{1j} = \sigma_j$ and $m_{2j} = \dot{\sigma}_j$ the corresponding state variables. In (26), $\bar{f}_j = f_{j_{\mathrm{nom}}} + \Delta f_j$, where $f_{j_{\mathrm{nom}}}$ is the ideal dynamic compensated by $u_{\theta_j}^{\mathrm{opt}}$, and $\Delta f_j$ is the 'disturbance' term, which is assumed to be Lipschitz continuous, *i.e.* $|\dot{\Delta f}_j| < O_j \in \mathbb{R}$, for all $(t, j) \in \mathbb{R}^+ \times \mathbb{N}_N$. Following Pérez-Ventura et al. (2021), each corresponding $u_{\theta_j}^{\mathrm{SMC}}$ is defined as

$$\begin{aligned}
u_{\theta_j}^{\mathrm{SMC}} &= -k_{1j}\lceil\sigma_j\rfloor^{1/3} - k_{2j}\lceil\dot{\sigma}_j\rfloor^{1/2} + \varphi_j\\
\dot{\varphi}_j &= -k_{3j}\lceil\sigma_j\rfloor^0,
\end{aligned} \tag{27}$$

with $\mathscr{K}_j^{\mathrm{SMC}} = \{k_{1j}, k_{2j}, k_{3j}\} \subset \mathbb{R}$ the set of PID SMC gains associated with the $j$-device. Then, for an appropriate design of $\mathscr{K}_j^{\mathrm{SMC}}$, the control law (27) stabilises the origin of the ideal model associated with (26) in finite-time (Pérez-Ventura et al., 2021), for every WEC device $j \in \mathbb{N}_N$ involved in the layout under analysis. The specific design procedure followed for experimental determination of the sets $\mathscr{K}_j^{\mathrm{SMC}}$ is detailed in Section 5.

## 5. Experimental results

Within this section, we provide a detailed analysis of the design, experimental implementation, and performance appraisal of the proposed SM$^2$C structure, for the totality of WEC array layouts described in Section 2.3, and the operating (sea state) conditions listed in Section 2.4. In particular, Section 5.1 illustrates the moment-based optimal reference generation procedure, providing detail on the different parameters established within problem $\widetilde{(\mathrm{P}_K)}$ in (17)–(18) for the real-time implementation of the technique. Section 5.2 provides a performance analysis of the inner tracking loop, based on the PID-SMC algorithm described in Section 4.2, including corresponding tuning of the set of gains $\mathscr{K}_j^{\mathrm{SMC}}$. Finally, Section 5.3 discusses the performance obtained with the overall SM$^2$C algorithm, for all tested layouts and sea state conditions generated within the basin, including a comparison with benchmark control strategy.

### 5.1. Moment-based reference generation

We begin by illustrating moment-based optimal reference generation, providing detail on the different parameters established within Problem $\widetilde{(\mathrm{P}_K)}$. Two different key quantities can change the performance and computational properties associated with the NP in (17)–(18), *i.e.* the fundamental frequency $\omega_0$, which is inherently linked to the time-window $T_\mathrm{h}$, and the number of harmonics describing the extended implicit form in (13). Tuning of these parameters is addressed in the following paragraphs, analogously to the procedure considered for a single device in Faedo et al. (2023).

Recall that the length of the time window $T_\mathrm{h} = 2\pi/\omega_0$ essentially defines the fundamental frequency in $\lambda(S)$ in (13). In other words, a larger $T_\mathrm{h}$ automatically implies a smaller $\omega_0$, which in turn describes a more refined 'frequency-step' in the computation of both $\widetilde{L_\theta}$ and $\widetilde{L_u}^{\mathrm{opt}}$, as per Eqs. (23) and (18), respectively. Nonetheless, note that the selection of $T_\mathrm{h}$ is also strongly linked to the final number of harmonics $\tilde{\nu}/2$ in (13), which effectively defines the corresponding approximation space for the optimal state and input variables (see Remark 4). This inherent trade-off between $T_\mathrm{h}$ and $\tilde{\nu}/2$ can be resolved, in practice, in terms of a single parameter, *i.e.* the so-called cut-off frequency $\omega_\mathrm{c} = (\tilde{\nu}/2)\omega_0$, which defines the largest multiple of $\omega_0$ used to describe the implicit form generator in (13). Following Faedo et al. (2023), the value of $\omega_\mathrm{c}$ can be determined (and fixed) a-priori, in terms of the largest frequency in which the stochastic description associated with the set of experimental sea states {ISS1, ISS2, ISS3} effectively present significant energy density. Having fixed the value of $\omega_\mathrm{c}$, and letting $\tilde{\nu}/2 = \mathrm{ceil}(T_\mathrm{h}\omega_\mathrm{c}/2\pi)$, the tuning procedure is approached in simulation by varying $T_\mathrm{h}$ accordingly, while monitoring both the value associated with the optimal objective value in $\widetilde{(\mathrm{P}_K)}$, and corresponding computational burden. Within this experimental campaign, the cut-off frequency is set to $\omega_\mathrm{c} = 15$ [rad/s], effectively covering (in frequency) the significant spectral density associated with all three tested sea states (see Fig. 4). The time horizon $T_\mathrm{h}$ is set to 10 [s], *i.e.* a fundamental frequency $\omega_0 \approx 0.63$ [rad/s], while the resulting final value for $\tilde{\nu}/2$ is 15, meaning that the QP in Eq. (18) is carried over $\mathbb{R}^{N\times 30N}$.

The moment-based generation sampling rate is set to 25 [Hz], *i.e.* a sampling time $\Delta_\mathrm{h} = 0.04$ [s], consistent with the experimental study in Faedo et al. (2023) and Ringwood et al. (2019). Note that, while real-time computation is effectively achieved for all the tested layouts within this experimental campaign, a centralised approach for the computation of the optimal reference profiles can become potentially unfeasible if a larger number of devices is effectively included within the control procedure. To circumvent this issue, a decentralised approach can be pursued, in the spirit of *e.g.* Li and Belmont (2014) and Ringwood et al. (2023), where local models are effectively used, which incorporate the most significant interactions between devices in the control computation procedure within a limited 'neighbourhood' of a given WEC.

The constraint set $\mathscr{C}$ in (10) is such that $U_{\max} = 12.5$ [N m], as per the specifications for this particular prototype adopted in Ringwood et al. (2019). Finally, the constraint map in (19)–(20) is performed with the collocation set $\mathcal{T} \subset \Xi_K$ defined with a (uniform) step of twice $\Delta_\mathrm{h}$, resulting in an associated cardinality of $N_c = T_\mathrm{h}/(2\Delta_\mathrm{h}) = 125$. Finally, note that, due to the definition of each time-window $\Xi_K$ as in (21), reference generation (and, hence, the overall SM$^2$C loop) is effectively started at $t_m = T_h/2 = 5$ [s], *i.e.* when $T_h/2$ [s] of available $f_\theta$ information becomes available.

Two different reference generation cases are considered within this experimental evaluation, namely decentralised and centralised (see the discussion provide in Section 1). Decentralised reference generation is performed by consistently using the optimal moment-based trajectories $\{u_\theta^{\mathrm{opt}}, z_\theta^{\mathrm{opt}}, v_\theta^{\mathrm{opt}}\}$ computed for L0 *only*, *i.e.* the single (standalone) device case, and propagated accordingly to each device composing the array under analysis, for each sea state tested within the basin. This decentralised case, clearly, uses the I/O model identified for L0, and hence ignores any interaction between adjacent devices, computing the optimal regime for the full array only based on the information of the dynamics associated with each standalone WEC system. In contrast, within the centralised case, each identified array model (as per Eq. (6)) is considered for the reference generation procedure, incorporating the interaction between adjacent systems, for each layout and sea state tested. Though the difference in performance (in terms of energy absorption) is explicitly addressed for decentralised and centralised cases within Section 5.3, we provide, in the following, a brief numerical appraisal on the results arising from the moment-based reference generation procedure for each of these scenarios.

In particular, Fig. 11 compares optimal reference generation (displacement), for the decentralised and centralised cases, when the L3 layout is used, for ISS3. Recall that the decentralised control is computed based on the dynamical model associated with L0, and propagated accordingly to all the devices composing the layout (D1, D2 and D3, for the L3 case). As can be appreciated within Fig. 11, while the computed optimal profiles for D1 and D3 (which are the two devices at the 'boundaries' of L3) can be considered to be relatively similar, the reference generation for D2 (*i.e.* the device in between D1 and D3) is significantly different for decentralised and centralised approaches. The centralised controller effectively considers the interaction between devices, which is particularly significant for the case of D2, given its (mid) position in the layout (see also the Bode plot in Fig. 5). As demonstrated experimentally, in Section 5.3, this difference in trajectory generation leads to suboptimal power absorption for the decentralised case, particularly close to the resonance frequency of the (standalone) device, where interactions between WEC systems in the layout can be potentially significant.

To complete the partial results presented in Fig. 11, Fig. 12 presents normalised mean average percentage accuracy (NMAPA) corresponding with each centralised reference generation (for L1, L2 and L3), defined in terms of (8) simply as $\mathrm{NMAPA}(f, f_{\mathrm{ref}}) = 100 - \mathrm{NMAPE}(f, f_{\mathrm{ref}})$, against the decentralised case (L0), considering each individual device composing the layouts (D1, D2 and D3), and sea states tested within the basin (ISS1, ISS2 and ISS3). As can be appreciated in Fig. 11, the computed moment-based optimal profiles can be significantly different depending on both the sea state, and the layout considered, with L3 being the most affected in terms of NMAPA (particularly for D2 — see the discussion provided in the paragraph immediately above). Note that L2, on average, presents more similar centralised optimal trajectories to those computed for L0 (*i.e.* in the decentralised case), since the devices in the two layouts are effectively more distant, creating smaller interaction between WECs, and hence presenting a higher degree of similarity with respect to the standalone counterpart.

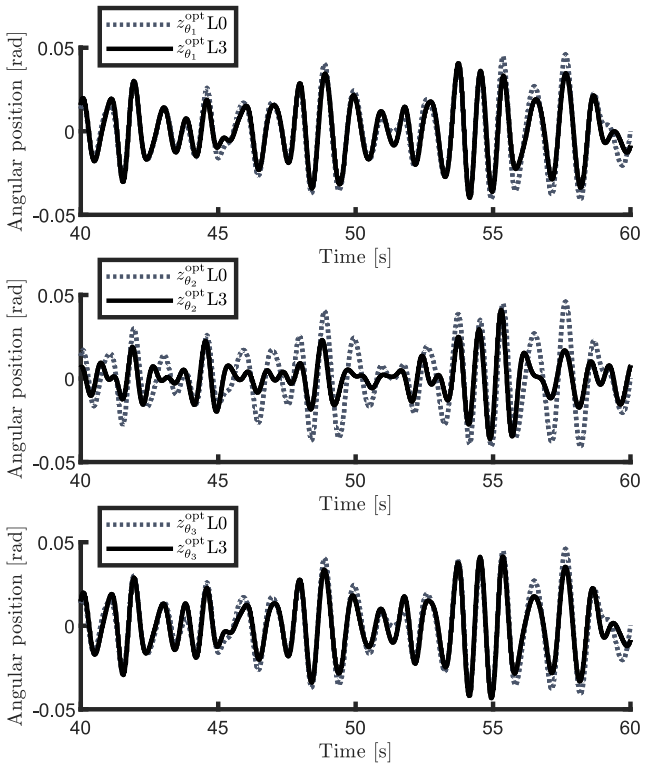


**Fig. 11.** Optimal reference generation (displacement), for the decentralised and centralised case, when L3 is considered within the basin (D1 to D3), for ISS3.

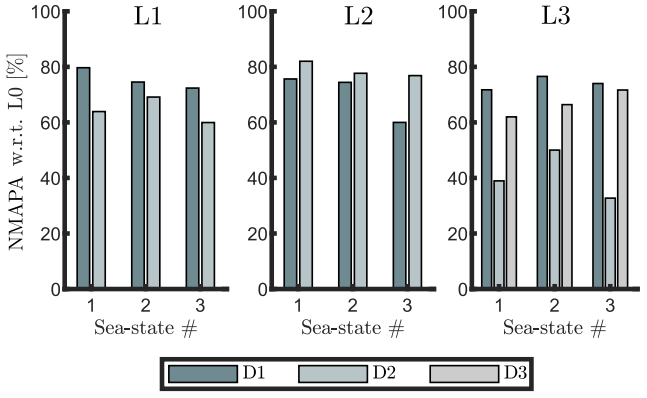


**Fig. 12.** NMAPA corresponding with each centralised generation (for L1, L2 and L3) against the decentralised case (L0), considering each individual device composing the layouts (D1, D2 and D3) and sea state tested within the basin (ISS1, ISS2 and ISS3).

### 5.2. PID-SMC controller

The PID-SMC control contribution, as defined in (27), has been tuned following the procedure described in Pérez-Ventura et al. (2021), using L0 as the benchmark case, *i.e.* the tracking control parameters in (27) are adjusted experimentally on a single prototype and propagated correspondingly to each device composing the array, that is $k_{ij} \equiv k_i$ for every $j \in \mathbb{N}_N$, with $i \in \mathbb{N}_3$. In this way, all the interaction between devices is handled at the optimal reference determination stage, using the centralised controller. In particular, $k_3$ is initially fixed to $k_3 = 1.1$, while $\{k_1, k_2\}$ are chosen analogously to a classic (standard) PID controller, *e.g.* to increase the rise time, reduce overshoot, and improve settling time. The final values for these two parameters are set to $k_1 = k_2 = 5$. To illustrate the performance of the corresponding SMC-based tracking loop, and corresponding convergence properties, Fig. 13 shows

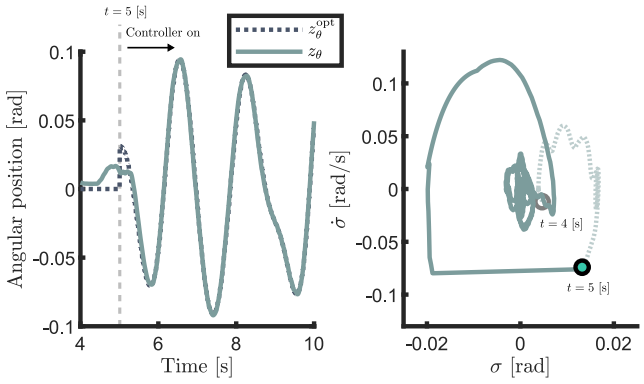


**Fig. 13.** Behaviour of the controlled system for the first five seconds (recall that the SM$^2$C is activated at $t = 5$ [s]).

the behaviour of the controlled system for the first five seconds (recall that the controller is activated at $t = 5$ [s] - see Section 5.1), for the case of L0, with sea state ISS2, in terms of reference and actual angular displacement, *i.e.* $z_\theta^{\text{opt}}$ and $z_\theta$, respectively. As can be appreciated in terms of device displacement, right after the controller is activated, the PID-SMC loop is capable of tracking the optimal reference $z_\theta^{\text{opt}}$ accordingly (left side of Fig. 13), the actual displacement being almost indistinguishable from the target motion after convergence. In fact, this can be further appreciated in the phase-plane $\sigma$-$\dot{\sigma}$ (right side of Fig. 13), where, following activation of the overall controller at $t = 5$ [s], convergence towards $\sigma = \dot{\sigma} = 0$ is rapidly achieved.

Following the results presented within Fig. 13, Fig. 14 offers a (longer) time snippet of the tracking performance for the case of L0, under ISS2, in terms of reference and actual angular displacement. As can be appreciated from the top figure, both target and WEC displacement are virtually indistinguishable from each other in a qualitative sense, while the bottom of Fig. 14 effectively illustrates normalised approximation error (in absolute value), having a corresponding mean value over the full sea state realisation of approximately 1%. To further complete the performance results for the tracking loop, and demonstrate the capabilities of the PID-SMC controller presented in Section 4.2, Fig. 15 illustrates tracking behaviour for the case of L3 (D1 to D3), when ISS1 is generated within the basin. Once again, reference and actual displacement are virtually identical, for all three devices involved in the WEC array configuration, further demonstrating the capabilities of the algorithm for the array layouts and sea states considered.

### 5.3. SM$^2$C performance assessment

Considering both the moment-based generation and PID-SMC tracking procedures, with the parameters and preliminary performances described within Sections 5.1 and 5.2, respectively, this section provides a detailed experimental performance assessment in terms of energy absorption for the overall control framework, *i.e.* SM$^2$C. This includes assessment for all the tested array layouts, in all the sea state conditions tested within the basin, for both decentralised and centralised optimal reference generation cases.

Before presenting the main results of this section, we note that a popular energy-maximising controller has been included as a benchmark case within this study, *i.e.* the so-called *passive* (proportional) WEC controller:

$$u_j^{\text{P}} = -P_j^{\text{P}} v_{\theta_j}, \tag{28}$$

with $u^{\text{P}}(t) \in \mathbb{R}^N$, and where the set $\mathscr{P}^{\text{P}} = \{P_j^{\text{P}}\}_{j \in \mathbb{N}_N} \subset \mathbb{R}^+$. In particular, as it is standard within the literature, the gains associated with the proportional controller in (28) are computed based on the dynamics of an isolated device, *i.e.* L0, and propagated accordingly to the $N$

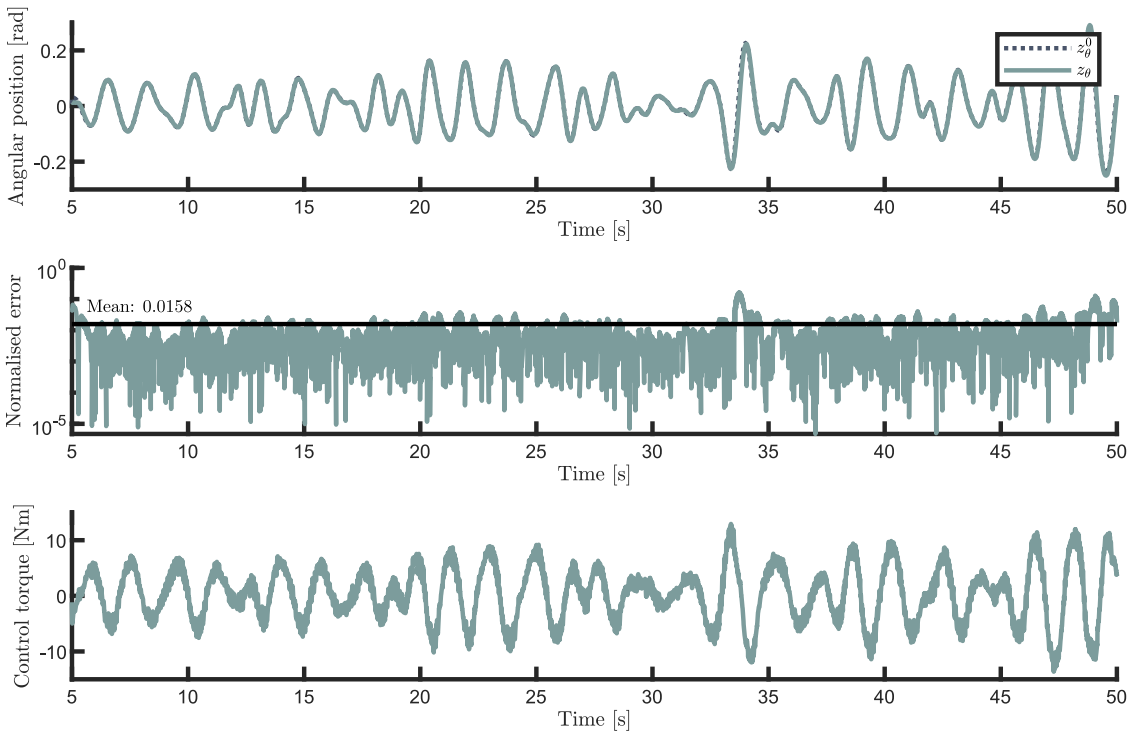


**Fig. 14.** Time snippet of the tracking performance for the case of L0, under ISS2, in terms of reference and actual angular displacement, *i.e.* $z_\theta^{\text{opt}}$ and $z_\theta$ (top), corresponding normalised error (centre), and associated control input (bottom).

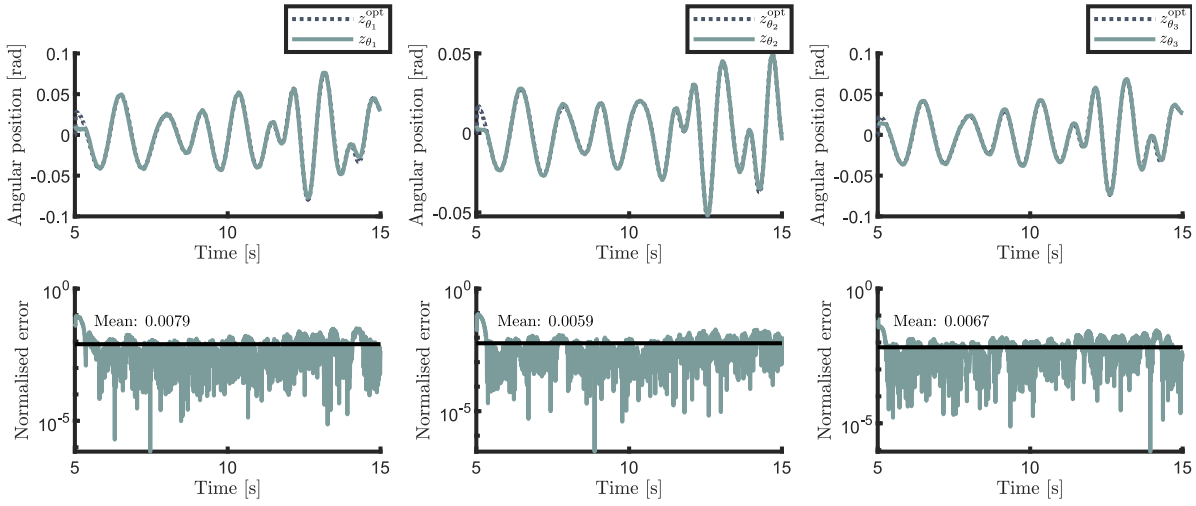


**Fig. 15.** Time snippet of the tracking performance for the case of L3 (D1 to D3), under ISS1, in terms of reference and actual angular displacement, *i.e.* $z_\theta^{\text{opt}}$ and $z_\theta$ (top), and corresponding normalised error.

devices composing the layout under analysis, that is $P_j^{\text{P}} = P_i^{\text{P}} \equiv P^{\text{P}}$ for all $(i, j) \in \mathbb{N}_N \times \mathbb{N}_N$. Furthermore, and aiming to provide the best-case scenario for the benchmark controller, the set $\mathscr{P}^{\text{P}}$ is changed (*i.e.* tuned) according to the sea state tested within the basin, according to the so-called impedance-matching principle: Leveraging the frequency response of the dynamical system (6) associated with L0, the value of $P^{\text{P}}$ can be computed (Faedo, Carapellese et al., 2022) as

$$P^{\text{P}} = |G_{\text{ID}-\theta}^{-1}(j\omega_p)|, \tag{29}$$

where $\omega_p$ is the frequency corresponding to the associated peak period for each tested sea state, *i.e.* $\omega_p = 2\pi/T_p$. A full appraisal of the specific values for $P^{\text{P}}$ is presented within Table 4.

Following introduction of the benchmark controller (28), Fig. 16 presents an overview of the experimental performance results obtained within this study, for all the tested layouts and sea states considered, in the case of decentralised and centralised SM$^2$C. In particular, two main performance metrics are presented within Fig. 16. Firstly, and directly following the control objective in (9), the mean absorbed energy for each full test is considered, *i.e.*

$$\mathscr{J} = -\frac{1}{T_{\text{test}}} \int_{\Xi} v_\theta^{\intercal} u \, \mathrm{d}t \ [\text{W}], \tag{30}$$

**Table 4**
Specific values for the passive (proportional) benchmark controller, according to each tested sea state.

| | ISS1 | ISS2 | ISS3 |
|---|---|---|---|
| $P^{\text{P}}$ [N m s/rad] | 9.57 | 16.74 | 2.81 |

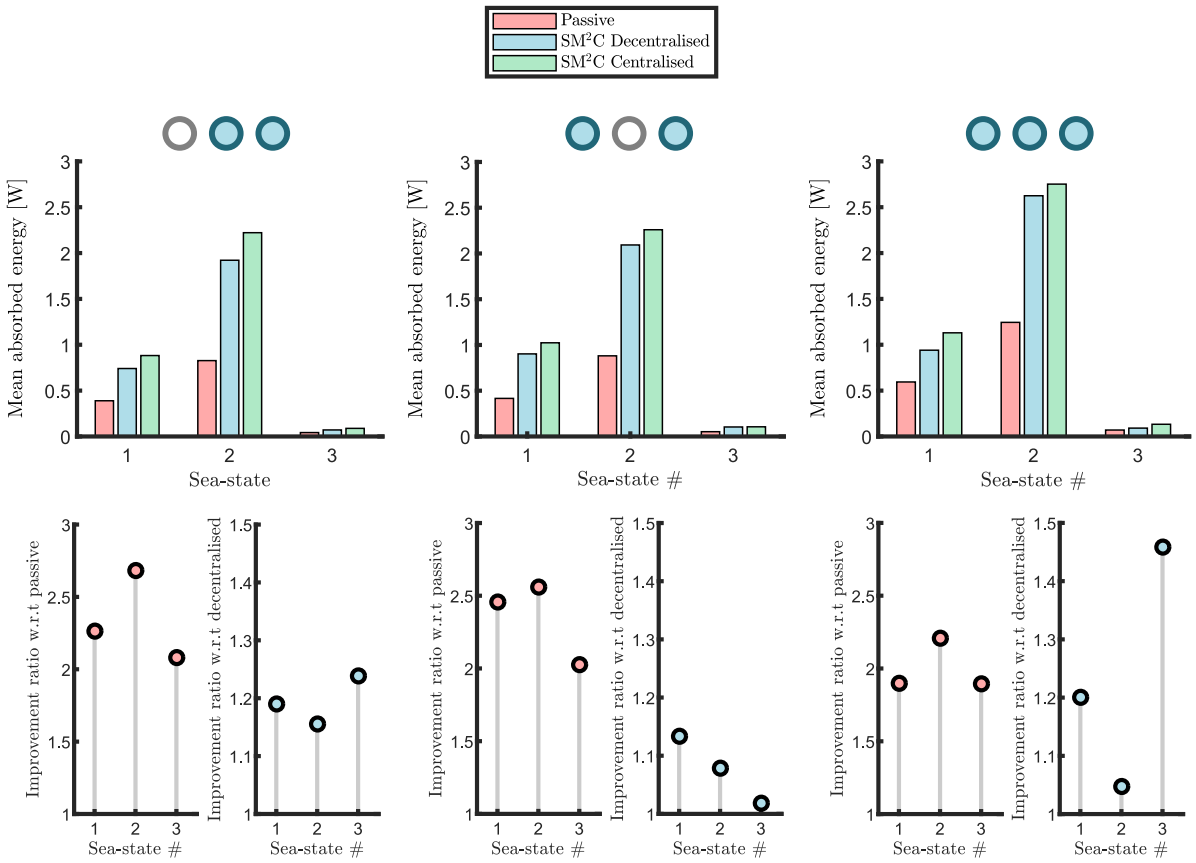


**Fig. 16.** Energy absorbed by each controller, for every layout and sea state tested (top). Improvement ratio obtained by considering the centralised SM$^2$C solution, with respect to the benchmark (passive) controller and decentralised SM$^2$C (bottom).

where $\Xi = [0, T_{\text{test}}]$, with $T_{\text{test}} = 300$ [s] (as indicated in Table 2). This is presented explicitly in Fig. 16 (top), for each layout (L1, L2 and L3), sea state, and control scenario considered. Clearly, the centralised SM$^2$C achieves the maximum energy absorption for all three layouts, in all tested sea states, demonstrating the importance of considering the interaction between devices in a given layout in order to effectively maximise energy capture from the resource. To further evaluate performance, we define the ratio between power absorption for passive and decentralised SM$^2$C controllers, and that provided by the centralised SM$^2$C solution. This is presented within Fig. 16 (bottom), for every single sea state and layout tested. Note that ratios of up to $\approx 2.8$ times in energy absorption can be obtained with respect to the benchmark (passive) controller by exploiting the centralised SM$^2$ solution, while up to $\approx 1.5$ more power can be absorbed when considering the interactions (using the centralised controller) within the design of the SM$^2$C, as opposed to the decentralised case. This is particularly marked for L3 and SS3 where, as discussed previously within Section 5.1, device D2 experiences significant interaction due to the motion of D1 and D2, particularly in the neighbourhood of the resonance frequency of the (standalone) system, which is precisely where SS3 has significant wave components (see Table 2).

Finally, and aiming to briefly illustrate motion under controlled conditions, Fig. 17 shows angular position, control torque, instantaneous power, angular velocity, and measured wave excitation force (as in Section 3.3). In particular, passive and centralised SM$^2$C are considered, when ISS1 is generated within the basin, for L1 (D1 and D2). It can be almost immediately appreciated that the SM$^2$C strategy, via optimal moment-based reference generation and subsequent robust PID-SMC tracking, exploits the operational space of the array considerably more efficiently than the benchmark (passive) counterpart, effectively presenting larger displacement and velocity trajectories, with an increase in power absorption. The control force applied by the SM$^2$C effectively presents typical sliding behaviour, though the chattering effect is ameliorated with respect to a standard sliding mode control, via the applied continuous sliding control torque (see Eq. (27)). Furthermore, the reactive nature of the centralised SM$^2$C can be appreciated immediately from Fig. 17, presenting negative instantaneous power values for specific time instants, required to 'enforce' resonance conditions with the incoming wave field. The benchmark controller, instead, is effectively passive, *i.e.* only positive instantaneous power values are attained. Note that the power flow is much larger for the optimal SM$^2$C, consistent with the improvement in overall energy absorption presented in Fig. 16. Finally, we note that the centralised SM$^2$C, in contrast to the benchmark passive controller case, is able to synchronise the instantaneous phase of angular velocity and wave excitation torque, as expected per standard optimal energy maximising conditions for WECs (see *e.g.* Faedo, Carapellese et al., 2022). This can be appreciated at the bottom of Fig. 17.

## 6. Conclusions

Motivated by the lack of a comprehensive experimental implementation and assessment of the potential benefit that can be achieved with energy-maximising optimal control solutions for WEC arrays, we present, within this paper, the development, design, experimental implementation, and performance appraisal, of optimal moment-based control for arrays of WEC systems, in both a centralised and decentralised fashion. Four different WEC array layout configurations are considered, with up to three 1:20 scale prototypes of the Wavestar WEC system operating simultaneously within the basin, subject to a variety of sea state conditions. In particular, the proposed SM$^2$C composite control structure, composed of a receding-horizon moment-based reference

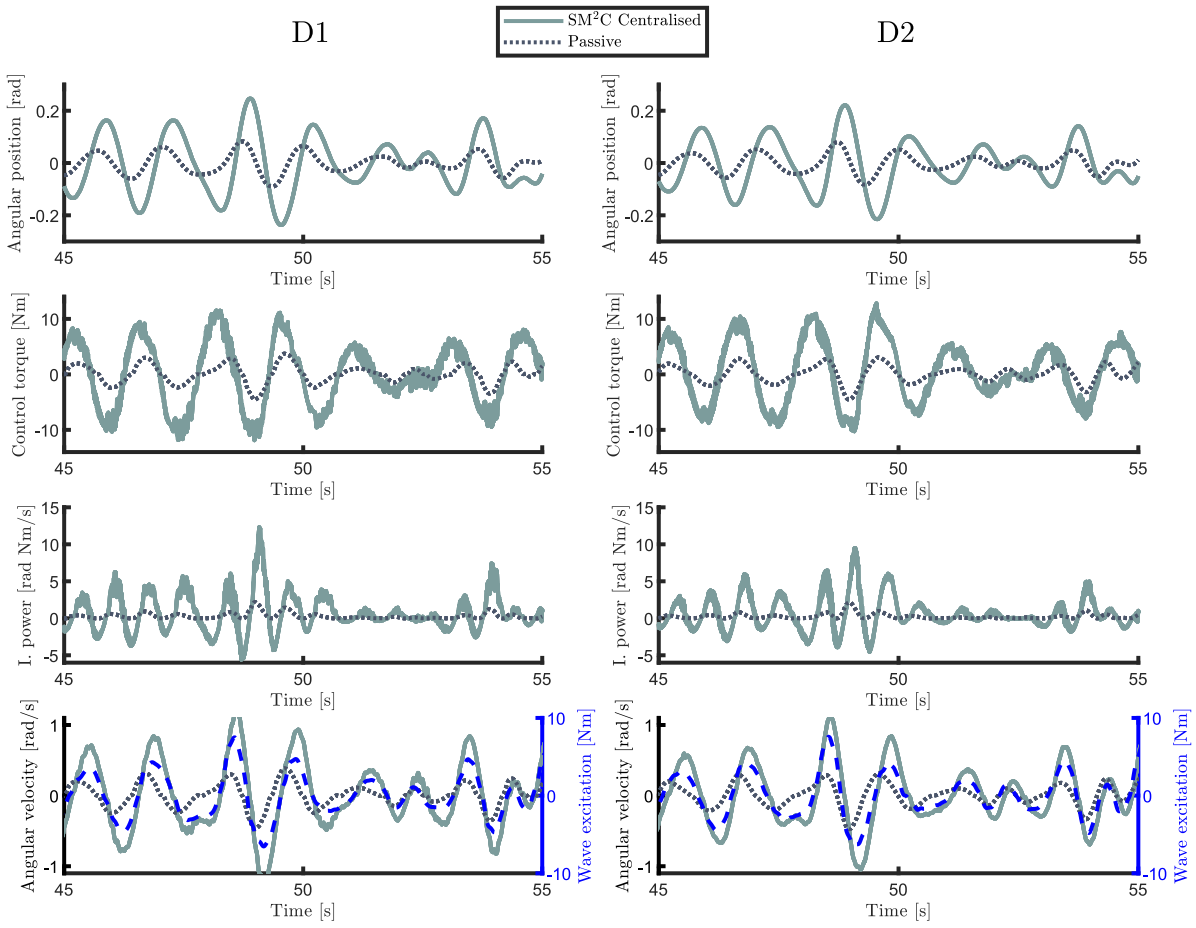


**Fig. 17.** Angular position, control torque, instantaneous power, angular velocity, and measured wave excitation force for passive and centralised SM$^2$C when ISS1 is generated within the basin, for L1 (D1 and D2).

generation procedure, and an associated PID-SMC tracking controller, is implemented and assessed experimentally, providing a detailed analysis of key performance metrics. We show that the proposed SM$^2$C strategy is able to maximise energy absorption for all the considered WEC array layouts, with up to 2.8 times energy improvement when compared to the benchmark controller case, while also consistently handling constraints within the definition of the associated OCP, for all the generated sea state conditions within the basin. The findings of this experimental study show tangible proof of the performance enhancement that can be achieved in arrays of WEC systems with the use of appropriate control technology, demonstrating not only the feasibility of the proposed SM$^2$C strategy in itself, but the key role that control systems have to play in the pathway towards effective exploitation of the yet largely untapped wave energy resource.

## Declaration of competing interest

The authors declare that they have no known competing financial interests or personal relationships that could have appeared to influence the work reported in this paper.

## Acknowledgements

The authors are grateful with Dr. M. Folley, from Queen's University Belfast, for his valuable input during the execution of the experimental campaign. The support of Dr. S. Wood, which has been fundamental for setup of the data acquisition system, is also appreciated by the authors. This project has received funding from the European Union's Horizon 2020 research and innovation programme under the Marie Sklodowska-Curie grant agreements No 101024372 and 101034297, and support from the framework COST Action 17105 - WECANet. The support of the Facultad de Ingeniería, Universidad Nacional de La Plata (UNLP), CONICET, and Agencia I+D+i from Argentina, is also acknowledged.

## References

Astolfi, Alessandro (2010). Model reduction by moment matching for linear and nonlinear systems. *IEEE Transactions on Automatic Control*, *55*(10), 2321–2336.

Astolfi, Alessandro, Scarciotti, Giordano, Simard, Joel, Faedo, Nicolás, & Ringwood, John V. (2020). Model reduction by moment matching: Beyond linearity a review of the last 10 years. In *2020 59th IEEE conference on decision and control (CDC)* (pp. 1–16). IEEE.

Babarit, Aurélien (2013). On the park effect in arrays of oscillating wave energy converters. *Renewable Energy*, *58*, 68–78.

Babarit, Aurélien, & Clément, Alain H. (2006). Optimal latching control of a wave energy device in regular and irregular waves. *Applied Ocean Research*, *28*(2), 77–91.

Bacelli, Giorgio, Balitsky, Philip, & Ringwood, John V. (2013). Coordinated control of arrays of wave energy devices—benefits over independent control. *IEEE Transactions on Sustainable Energy*, *4*(4), 1091–1099.

Bacelli, Giorgio, & Ringwood, John (2013). Constrained control of arrays of wave energy devices. *International Journal of Marine Energy*, *3*, e53–e69.

Boyd, Stephen, & Vandenberghe, Lieven (2004). *Convex optimization*. Cambridge University Press.

Brewer, John (1978). Kronecker products and matrix calculus in system theory. *IEEE Transactions on Circuits and Systems*, *25*(9), 772–781.

Carapellese, Fabio, Pasta, Edoardo, Paduano, Bruno, Faedo, Nicolás, & Mattiazzo, Giuliana (2022). Intuitive lti energy-maximising control for multi-degree of freedom wave energy converters: the pewec case. *Ocean Engineering*, *256*, Article 111444.

Chen, Weixing, Gao, Feng, Meng, Xiangdun, & Fu, Jianxun (2016). Design of the wave energy converter array to achieve constructive effects. *Ocean Engineering*, *124*, 13–20.

Chui, Charles K., Chen, Guanrong, et al. (2017). *Kalman filtering*. Springer.

Copping, Andrea E., Hemery, Lenaïg G., Overhus, Dorian M., Garavelli, Lysel, Freeman, Mikaela C., Whiting, Jonathan M., et al. (2020). Potential environmental effects of marine renewable energy development—the state of the science. *Journal of Marine Science and Engineering*, *8*(11), 879.

Davidson, Josh, Giorgi, Simone, & Ringwood, John V. (2015). Linear parametric hydrodynamic models for ocean wave energy converters identified from numerical wave tank experiments. *Ocean Engineering*, *103*, 31–39.

De Andrés, A. D., Guanche, R., Meneses, L., Vidal, C., & Losada, I. J. (2014). Factors that influence array layout on wave energy farms. *Ocean Engineering*, *82*, 32–41.

Energy Information Administration (EIA) (2019). *International energy outlook*: *Technical report*, Washington, United States: EIA.

European Commission (2011). *Energy roadmap 2050: Impact assessment and scenario analysis*: *Technical report*, Brussels, Belgium: European Commission.

European Commission (2014). *A policy framework for climate and energy in the period 2020 to 2030*: *Technical report*, Brussels, Belgium: European Commission.

European Commission (2019). *The European green deal*: *Technical report*, Brussels, Belgium: European Commission.

European Commission (2022). *Repowereu*: *Technical report*, Brussels, Belgium: European Commission.

Evans, D. V. (1979). Some theoretical aspects of three-dimensional wave-energy absorbers. In *Proc. 1st symp. wave energy utilization* (pp. 78–112).

Faedo, Nicolás (2021). LMI-based passivation for LTI systems with application to marine structures - Matlab implementation. URL https://doi.org/10.5281/zenodo.5797733.

Faedo, Nicolás, Carapellese, Fabio, Pasta, Edoardo, & Mattiazzo, Giuliana (2022). On the principle of impedance-matching for underactuated wave energy harvesting systems. *Applied Ocean Research*, *118*, Article 102958.

Faedo, Nicolás, García-Violini, Demián, Peña-Sanchez, Yerai, & Ringwood, John V. (2020). Optimisation-vs. non-optimisation-based energy-maximising control for wave energy converters: A case study. In *2020 European control conference (ECC)* (pp. 843–848). IEEE.

Faedo, Nicolás, García-Violini, Demián, Scarciotti, Giordano, Astolfi, Alessandro, & Ringwood, John V. (2019). Robust moment-based energy-maximising optimal control of wave energy converters. In *2019 IEEE 58th conference on decision and control (CDC)* (pp. 4286–4291). IEEE.

Faedo, Nicolás, Giorgi, G., Ringwood, J. V., & Mattiazzo, Giuliana (2022). Optimal control of wave energy systems considering nonlinear froude–krylov effects: control-oriented modelling and moment-based control. *Nonlinear Dynamics*, *109*(3), 1777–1804.

Faedo, Nicolás, Mosquera, Facundo D., Evangelista, Carolina A., Ringwood, John V., & Puleston, Paul F. (2022). Preliminary experimental assessment of second-order sliding mode control for wave energy conversion systems. In *2022 Australian & New Zealand control conference (ANZCC)* (pp. 63–68). IEEE.

Faedo, Nicolás, Olaya, Sébastien, & Ringwood, John V. (2017). Optimal control, mpc and mpc-like algorithms for wave energy systems: An overview. *IFAC Journal of Systems and Control*, *1*, 37–56.

Faedo, Nicolás, Pasta, Edoardo, Carapellese, Fabio, Orlando, Vincenzo, Pizzirusso, Domenica, Basile, Dario, et al. (2022). Energy-maximising experimental control synthesis via impedance-matching for a multi degree-of-freedom wave energy converter. *IFAC-PapersOnLine*, *55*(31), 345–350.

Faedo, Nicolás, Peña-Sanchez, Yerai, Carapellese, Fabio, Mattiazzo, Giuliana, & Ringwood, John V. (2021). Lmi-based passivation of lti systems with application to marine structures. *IET Renewable Power Generation*, *15*(14), 3424–3433.

Faedo, Nicolás, Peña-Sanchez, Yerai, García-Violini, Demián, Ferri, Francesco, Mattiazzo, Giuliana, & Ringwood, John V. (2023). Experimental assessment and validation of energy-maximising moment-based optimal control for a prototype wave energy converter. *Control Engineering Practice*, *133*, Article 105454.

Faedo, Nicolás, Peña-Sanchez, Yerai, & Ringwood, John V. (2020). Receding-horizon energy-maximising optimal control of wave energy systems based on moments. *IEEE Transactions on Sustainable Energy*, *12*(1), 378–386.

Faedo, Nicolás, Scarciotti, Giordano, Astolfi, Alessandro, & Ringwood, John V. (2018). Energy-maximising control of wave energy converters using a moment-domain representation. *Control Engineering Practice*, *81*, 85–96.

Faedo, Nicolás, Scarciotti, Giordano, Astolfi, Alessandro, & Ringwood, John V. (2019). Moment-based constrained optimal control of an array of wave energy converters. In *2019 American control conference (ACC)* (pp. 4797–4802). IEEE.

Faedo, Nicolás, Scarciotti, Giordano, Astolfi, Alessandro, & Ringwood, John V. (2021a). Energy-maximising moment-based constrained optimal control of ocean wave energy farms. *IET Renewable Power Generation*, *15*(14), 3395–3408.

Faedo, Nicolás, Scarciotti, Giordano, Astolfi, Alessandro, & Ringwood, John V. (2021b). On the approximation of moments for nonlinear systems. *IEEE Transactions on Automatic Control*, *66*(11), 5538–5545.

Falcao, Antonio (2002). Wave-power absorption by a periodic linear array of oscillating water columns. *Ocean Engineering*, *29*(10), 1163–1186.

Garcia-Rosa, Paula B., Bacelli, Giorgio, & Ringwood, John V. (2015). Control-informed optimal array layout for wave farms. *IEEE Transactions on Sustainable Energy*, *6*(2), 575–582.

García-Violini, Demián, Peña-Sanchez, Yerai, Faedo, Nicolás, Ferri, Francesco, & Ringwood, John V. (2023). A broadband time-varying energy maximising control for wave energy systems (lite-con+): Framework and experimental assessment. *IEEE Transactions on Sustainable Energy*.

Göteman, Malin, Giassi, Marianna, Engström, Jens, & Isberg, Jan (2020). Advances and challenges in wave energy park optimization—a review. *Frontiers in Energy Research*, *8*, 26.

Gunn, Kester, & Stock-Williams, Clym (2012). Quantifying the global wave power resource. *Renewable Energy*, *44*, 296–304.

Guo, Bingyong, & Ringwood, John V. (2021). A review of wave energy technology from a research and commercial perspective. *IET Renewable Power Generation*, *15*(14), 3065–3090.

Hansen, Rico Hjerm, & Kramer, Morten M. (2011). Modelling and control of the wavestar prototype. In *9th European wave and tidal energy conference (EWTEC)* (pp. 1–10). Southampton.

Hasselmann, Dieter E., Dunckel, M., & Ewing, J. A. (1980). Directional wave spectra observed during jonswap 1973. *Journal of Physical Oceanography*, *10*(8), 1264–1280.

Heo, Sanghwan, & Koo, Weoncheol (2021). Dynamic response analysis of a wavestar-type wave energy converter using augmented formulation in korean nearshore areas. *Processes*, *9*(10), 1721.

Hodges, J., Henderson, J., Ruedy, L., Soede, M., Weber, J., Ruiz-Minguela, P., et al. (2021). *An international evaluation and guidance framework for ocean energy technology*: *Technical report*, Lisbon, Portugal: International Energy Agency - Ocean Energy Systems (IEA-OES.

Kurnia, R., & Ducrozet, G. NEMOH V3.0 user manual. Ecole Centrale de Nantes.

Langhamer, Olivia, Haikonen, Kalle, & Sundberg, Jan (2010). Wave power—sustainable energy or environmentally costly? a review with special emphasis on linear wave energy converters. *Renewable and Sustainable Energy Reviews*, *14*(4), 1329–1335.

Li, Guang, & Belmont, Mike R. (2014). Model predictive control of sea wave energy converters–part ii: The case of an array of devices. *Renewable Energy*, *68*, 540–549.

Ljung, Lennart (1999). *System identification*. Prentice Hall.

López, Iraide, Andreu, Jon, Ceballos, Salvador, Alegría, Iñigo Martínez De, & Kortabarria, Iñigo (2013). Review of wave energy technologies and the necessary power-equipment. *Renewable and Sustainable Energy Reviews*, *27*, 413–434.

Marquez, Horacio J. (2003). *Nonlinear control systems: analysis and design, Vol. 161*. John Wiley Hobokenˆ eN. JNJ.

McCormick, Michael E. (2013). *Ocean wave energy conversion*. Courier Corporation.

McKechan, D. J. A., Robinson, C., & Sathyaprakash, Bangalore Suryanarayana (2010). A tapering window for time-domain templates and simulated signals in the detection of gravitational waves from coalescing compact binaries. *Classical and Quantum Gravity*, *27*(8), Article 084020.

McKelvey, Tomas, Akçay, Hüseyin, & Ljung, Lennart (1996). Subspace-based multivariable system identification from frequency response data. *IEEE Transactions on Automatic control*, *41*(7), 960–979.

Mérigaud, Alexis, & Ringwood, John V. (2017). Free-surface time-series generation for wave energy applications. *IEEE Journal of Oceanic Engineering*, *43*(1), 19–35.

Mork, Gunnar, Barstow, Stephen, Kabuth, Alina, & Pontes, M. Teresa (2010). Assessing the global wave energy potential. In *International conference on offshore mechanics and arctic engineering, Vol. 49118* (pp. 447–454).

Mosquera, F. D., Faedo, N., Evangelista, C. A., Puleston, P. F., & Ringwood, J. V. (2022). Energy-maximising tracking control for a nonlinear heaving point absorber system commanded by second order sliding modes. *IFAC-PapersOnLine*, *55*(31), 357–362.

Ochi, Michel K. (1998). *Cambridge ocean technology series*, *Ocean waves: The stochastic approach*. Cambridge University Press.

Oetinger, Daniela, Magaña, Mario E., & Sawodny, Oliver (2015). Centralised model predictive controller design for wave energy converter arrays. *IET Renewable Power Generation*, *9*(2), 142–153.

Papillon, Louis, Costello, Ronan, & Ringwood, John V. (2020). Boundary element and integral methods in potential flow theory: A review with a focus on wave energy applications. *Journal of Ocean Engineering and Marine Energy*, *6*, 303–337.

Pérez-Ventura, Ulises, Mendoza-Avila, Jesús, & Fridman, Leonid (2021). Design of a proportional integral derivative-like continuous sliding mode controller. *International Journal of Robust and Nonlinear Control*, *31*(9), 3439–3454.

Prabhu, K. M. Muraleedhara (2013). *Window functions and their applications in signal processing*. CRC Press.

Ransley, E. J., Greaves, D. M., Raby, A., Simmonds, D., Jakobsen, Morten Møller, & Kramer, M. (2017). RANS-VOF modelling of the wavestar point absorber. *Renewable Energy*, *109*, 49–65.

Reguero, B. G., Losada, I. J., & Méndez, F. J. (2015). A global wave power resource and its seasonal, interannual and long-term variability. *Applied Energy*, *148*, 366–380.

Ringwood, John V. (2020). Wave energy control: status and perspectives 2020. *IFAC-PapersOnLine*, *53*(2), 12271–12282.

Ringwood, John V. (2022). Marine renewable energy devices and their control: An overview. *IFAC-PapersOnLine*, *55*(31), 136–141.

Ringwood, John V., Bacelli, Giorgio, & Fusco, Francesco (2014). Energy-maximizing control of wave-energy converters: The development of control system technology to optimize their operation. *IEEE Control Systems Magazine*, *34*(5), 30–55.

Ringwood, John, Ferri, Francesco, Tom, Nathan, Ruehl, Kelley, Faedo, Nicolás, Bacelli, Giorgio, et al. (2019). The wave energy converter control competition: Overview. In *International conference on offshore mechanics and arctic engineering, Vol. 58899*. American Society of Mechanical Engineers, V010T09A035.

Ringwood, John V., Zhan, Siyuan, & Faedo, Nicolás (2023). Empowering wave energy with control technology: Possibilities and pitfalls. *Annual Reviews in Control*.

Robertson, Bryson, Hiles, Clayton, Luczko, Ewelina, & Buckham, Bradley (2016). Quantifying wave power and wave energy converter array production potential. *International Journal of Marine Energy*, *14*, 143–160.

Ross, David (1995). *Power from the waves*. USA: Oxford University Press.

Ruehl, Kelley, & Bull, Diana (2012). Wave energy development roadmap: Design to commercialization. In *2012 oceans* (pp. 1–10).

Sasaki, Wataru (2017). Predictability of global offshore wind and wave power. *International Journal of Marine Energy*, *17*, 98–109.

Speedgoat real-time target machines. (2023). https://it.mathworks.com/products/connections/product_detail/speedgoat-real-time-target-machines.html. Accessed: 2023-02-10.

Stratigaki, Vasiliki, Troch, Peter, Stallard, Tim, Forehand, David, Kofoed, Jens Peter, Folley, Matt, et al. (2014). Wave basin experiments with large wave energy converter arrays to study interactions between the converters and effects on other users in the sea and the coastal area. *Energies*, *7*(2), 701–734.

Taghipour, Reza, Perez, Tristan, & Moan, Torgeir (2008). Hybrid frequency–time domain models for dynamic response analysis of marine structures. *Ocean Engineering*, *35*(7), 685–705.

Thomas, Simon, Eriksson, Mikael, Göteman, Malin, Hann, Martyn, Isberg, Jan, & Engström, Jens (2018). Experimental and numerical collaborative latching control of wave energy converter arrays. *Energies*, *11*(11), 3036.

Thomas, G. P., & Evans, D. V. (1981). Arrays of three-dimensional wave-energy absorbers. *Journal of Fluid Mechanics*, *108*, 67–88.

Tom, Nathan, Ruehl, Kelley, & Ferri, Francesco (2018). Numerical model development and validation for the wecccomp control competition. In *International conference on offshore mechanics and arctic engineering, Vol. 51319*. American Society of Mechanical Engineers, V010T09A042.

Tona, Paolino, Sabiron, Guillaume, Nguyen, Hoai-Nam, Mérigaud, Alexis, & Ngo, Caroline (2020). Experimental assessment of the ifpen solution to the wec control competition. In *International conference on offshore mechanics and arctic engineering, Vol. 84416*. American Society of Mechanical Engineers, V009T09A023.

Trueworthy, Ali, & DuPont, Bryony (2020). The wave energy converter design process: Methods applied in industry and shortcomings of current practices. *Journal of Marine Science and Engineering*, *8*(11), 932.

Utkin, Vadim I. (2013). *Sliding modes in control and optimization*. Springer Science & Business Media.

Vavasis, Stephen A. (2001). *Complexity theory: Quadratic programming* (pp. 304–307). Springer US.

Vervaet, Timothy, Stratigaki, Vasiliki, Ferri, Francesco, Beule, Louis De, Claerbout, Hendrik, Witte, Bono De, et al. (2022). Experimental modelling of an isolated wecfarm real-time controllable heaving point absorber wave energy converter. *Journal of Marine Science and Engineering*, *10*(10), 1480.

VTI ingeniería. (2023). https://www.vtisl.com/en/test-systems/wave-laboratories/. Accessed: 2023-02-10.

Westphalen, J., Bacelli, Giorgio, Balitsky, Philip, & Ringwood, John (2011). Control strategies for arrays of wave energy devices. In *Proc. 9th European wave and tidal energy conf. (EWTEC)*. Southampton.

Windt, Christian, Faedo, Nicolás, García-Violini, Demián, Peña-Sanchez, Yerai, Davidson, Josh, Ferri, Francesco, et al. (2020). Validation of a cfd-based numerical wave tank model of the 1/20th scale wavestar wave energy converter. *Fluids*, *5*(3), 112.

Windt, Christian, Faedo, Nicolás, Penalba, Markel, Dias, Frederic, & Ringwood, John V. (2021). Reactive control of wave energy devices–the modelling paradox. *Applied Ocean Research*, *109*, Article 102574.

Zhang, Bo, Zhang, Haixu, Yang, Sheng, Chen, Shiyu, Bai, Xiaoshan, & Khan, Awais (2022). Predictive control for a wave-energy converter array based on an interconnected model. *Journal of Marine Science and Engineering*, *10*(8), 1033.

Zhong, Qian, & Yeung, Ronald W. (2019). Model-predictive control strategy for an array of wave-energy converters. *Journal of Marine Science and Application*, *18*, 26–37.

Zhong, Qian, & Yeung, Ronald W. (2022). On optimal energy-extraction performance of arrays of wave-energy converters, with full consideration of wave and multi-body interactions. *Ocean Engineering*, *250*, Article 110863.

Zurkinden, Andrew Stephen, Ferri, Francesco, Beatty, S., Kofoed, Jens Peter, & Kramer, M. M. (2014). Non-linear numerical modeling and experimental testing of a point absorber wave energy converter. *Ocean Engineering*, *78*, 11–21.